NeuroImage 52 (2010) 142–157

Contents lists available at ScienceDirect

NeuroImage

journal homepage: www.elsevier.com/locate/ynimg

Spectral-based automatic labeling and refining of human cortical sulcal curves using expert-provided examples

Ilwoo Lyu [a], Joon-Kyung Seong [a,*], Sung Yong Shin [a], Kiho Im [b], Jee Hoon Roh [d], Min-Jeong Kim [d], Geon Ha Kim [d], Jong Hun Kim [d], Alan C. Evans [c], Duk L. Na [d], Jong-Min Lee [b]

[a] Computer Science Department, KAIST, South Korea
[b] Department of Biomedical Engineering, Hanyang University, South Korea
[c] McConnell Brain Imaging Centre, Montreal Neurological Institute, McGill University, Montreal, QC, Canada H3A 2B4
[d] Department of Neurology, Sungkyunkwan University, Samsung Medical Center, 50 Ilwon-dong, Kangnam-ku, Seoul 135-710, South Korea

ARTICLE INFO

Article history:
Received 25 November 2009
Revised 26 February 2010
Accepted 26 March 2010
Available online 2 April 2010

Keywords:
Sulcal curve
Labeling
Refining
Spectral matching
Sulcal variability

ABSTRACT

We present a spectral-based method for automatically labeling and refining major sulcal curves of a human cerebral cortex. Given a set of input (unlabeled) sulcal curves automatically extracted from a cortical surface and a collection of expert-provided examples (labeled sulcal curves), our objective is to identify the input major sulcal curves and assign their neuroanatomical labels, and then refines these curves based on the expert-provided example data, without employing any atlas-based registration scheme as preprocessing. In order to construct the example data, neuroanatomists manually labeled a set of 24 major sulcal curves (12 each for the left and right hemispheres) for each individual subject according to a precise protocol. We collected 30 sets of such curves from 30 subjects. Given the raw input sulcal curve set of a subject, we choose the most similar example curve to each input curve in the set to label and refine the latter according to the former. We adapt a spectral matching algorithm to choose the example curve by exploiting the sulcal curve features and their relationship. The high dimensionality of sulcal curve data in spectral matching is addressed by using their multi-resolution representations, which greatly reduces time and space complexities. Our method provides consistent labeling and refining results even under high variability of cortical sulci across the subjects. Through experiments we show that the results are comparable in accuracy to those done manually. Most output curves exhibited accuracy values higher than 80%, and the mean accuracy values of the curves in the left and the right hemispheres were 84.69% and 84.58%, respectively.

Introduction

Sulcal and gyral folding patterns are principal landmarks of a human cerebral cortex, which are related to brain functions and functional regions (Dubois et al., 2008; Fischl et al., 2008; Im et al., 2010). Sulcal landmarks have played key roles in brain model registration (Hellier and Barillot, 2003), in discovering brain diseases and monitoring brain growth (Cachia et al., 2008; Thompson et al., 2004; Seong et al., 2010), and in measuring brain variability (Thompson et al., 1996a; Lohmann et al., 1999; Fillard et al., 2007; Im et al., 2010). Thus, labeling these landmarks is important for analysis of functional and structural neuroimaging data.

Many geometric methods dealt with extraction of sulcal landmarks by exploiting geometric information such as isotropic geodesic distance maps (Shi et al., 2008), sulcal depth maps (Kao et al., 2007), curvature-based folding measures (Batchelor and Castellano Smith, 2002; Rodriguez-Carranza et al., 2006; Pienaar and Fischl, 2008), and anisotropic geodesic maps (Seong et al., 2010). However, none of these methods addressed the issue of labeling given raw input sulci while refining them. Moreover, the geometry-based approach cannot distinguish the primary cortical sulci effectively from the secondary or tertiary sulci. The primary sulci in sulcal fundic regions are more consistent and invariant across different brains, which are useful in neuroimaging applications (Perrot et al., 2008; Im et al., 2010). Cortical parcellation methods for analyzing structural neuroimaging data (Rademacher et al., 1992; Caviness et al., 1996) may not be employed to address the issue of refining sulcal curves either, due to lack of neuroanatomical conventions.

Based on neuroanatomical and geometric information on a cortical surface, Fischl et al. (2004) presented a technique for parcellating the entire surface into gyral regions. FreeSurfer can also be used for cortical surface segmentation. In principle, labeled sulcal curves could be computed using these tools since sulcal curves are the common boundaries of gyral regions. In practice, however, it is nontrivial to segment the common boundaries into sulcal curves by identifying their end points. Moreover, as pointed out in Fischl et al. (2004), the

* Corresponding author.
E-mail address: seong@kaist.ac.kr (J.-K. Seong).

1053-8119/$ – see front matter © 2010 Elsevier Inc. All rights reserved.
doi:10.1016/j.neuroimage.2010.03.076

parcellation results exhibit large variations along sulcal regions, which makes it difficult to accurately trace sulcal curves along fundic regions of high curvature.

For labeling cortical features, Sandor and Leahy (1997) used a manually labeled brain atlas. An atlas encodes neuroanatomical labeling conventions determined by knowledge on structure–function relationships, and cytoarchitectronic or receptor labeling properties of regions, but lacks in geometrical details of individual cortical surfaces. Their approach warps the atlas to an individual subject's cortical surface in order to inherit the labels of cortical features from the atlas. Since this method depends on an atlas registration scheme, the geometric variability of each individual subject's cortical surface was neither exploited fully nor used to refine the cortical features. Similar surface-fitting methods have been reported in Vaillant et al. (1996), Thompson et al. (1996b), Lohmann (1998), Lohmann and von Cramon (2000) and Tao et al. (2002). Unlike these methods, our approach does not employ any atlas-based registration scheme as preprocessing.

A graph-based approach was taken in Goualher et al. (1999) and Mangin et al. (1995). In this approach, cortical sulci were represented by nodes, while their relationships were represented by arcs. The detected sulci were then labeled semi-automatically based on a training set which was prepared manually. This approach was further extended to detection of major cortical sulci, in which joint sulcal shape priors between neighboring sulci were used in the learning process (Shi et al., 2009). However, the approach simplified the sulcus detection problem by removing sulcal curves crossing over gyral regions and representing each sulcus as a simple curve. A watershed transform-based approach was presented in Lohmann (1998) and Rettmann et al. (2002), in which segmented regions were manually labeled by an expert. Learning-based techniques were also proposed in Riviere et al. (2002), Behnke et al. (2003), Tu et al. (2007), and Perrot et al. (2008) to detect and label sulci, which depend on specific atlas registration schemes (Riviere et al., 2002; Behnke et al., 2003; Perrot et al., 2008) or suffer from lacks of neuroanatomical conventions (Tu et al., 2007). Graph-based learning techniques were integrated into a public-domain system BrainVisa (Riviere et al., 2003), and cortical sulci that were detected or labeled by this system have been successfully used in many neuroimaging applications (Cachia et al., 2008; Cykowski et al., 2008a,b; Dubois et al., 2008; Douaud et al., 2009).

In this paper, a sulcus is represented as a sequence of (possibly disconnected) curve segments that follows the deepest part of the sulcal region. Ideally, sulcal curves should not only convey neuroanatomical conventions but also reflect individual variability of cortical surface geometry across subjects. However, the individual geometric variability makes it difficult to label brain structures as pointed out in Fischl et al. (2002), Pitiot et al. (2004) and Fillard et al. (2007). We present an automated method for labeling and refining sulcal curves of a human cerebral cortex: Given a set of input (unlabeled) sulcal curves of a subject and a collection of expert-provided examples (labeled sulcal curves), this method labels the input curves automatically extracted from a cortical surface while also refining these curves, according to neuroanatomical conventions conveyed by the examples. Our objective is to label and refine the input curves so as to reflect not only neuroanatomical conventions but also individual variability of cortical surface geometry. The input sulcal curves are extracted automatically from a cortical surface by using the method in (Seong et al., 2010), and the expert-provided examples are prepared manually by neuroanatomists according to a precise protocol. For experiments, we used a set of 24 major sulcal curves (12 each for the left and the right hemispheres) from each subject in the example database, and collected 30 sets of such curves from 30 different subjects (Fig. 1). Extracted automatically based on pure geometric

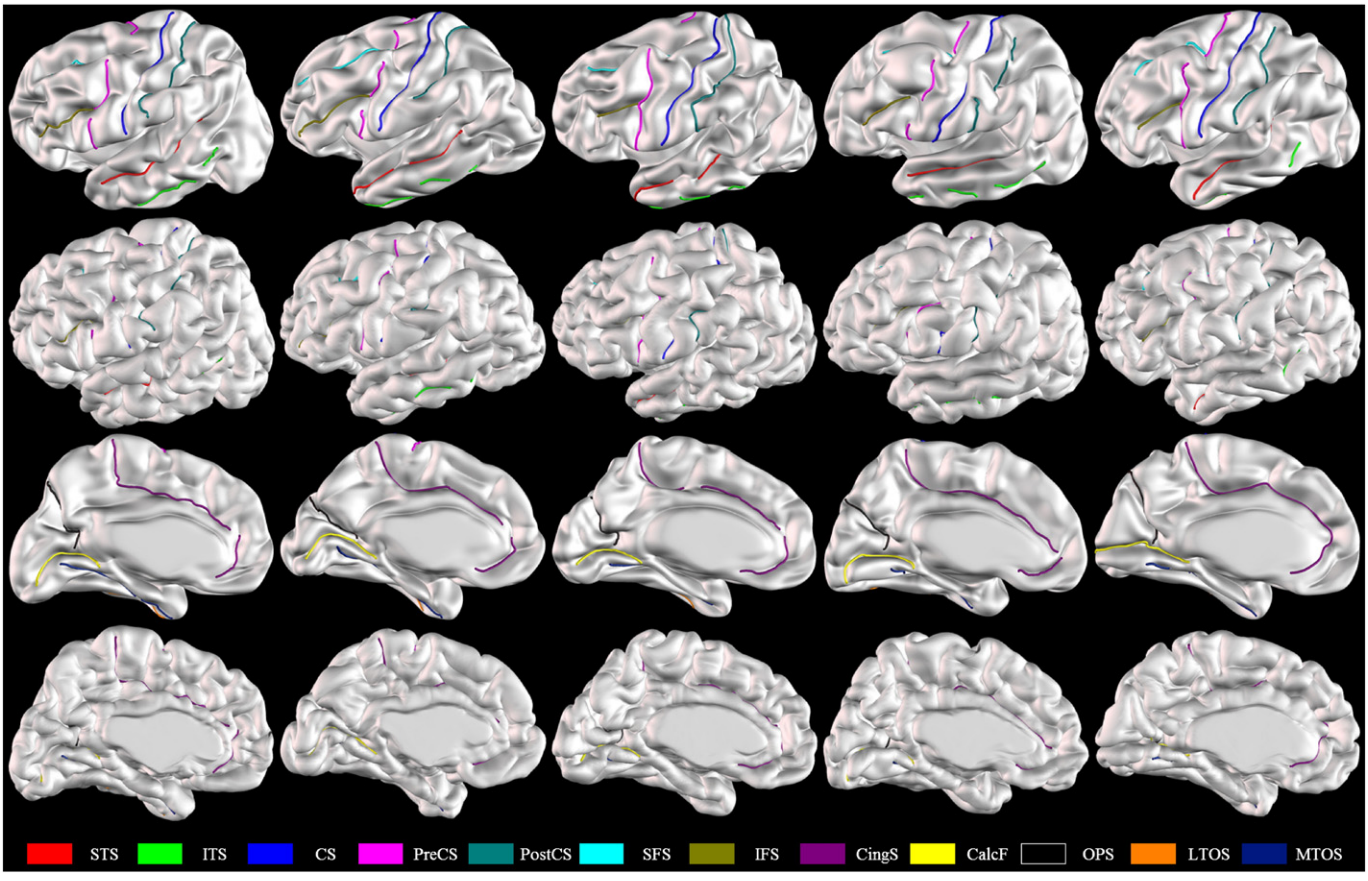

Fig. 1. Lateral and medial regions of five sample left hemispheres with manually extracted sulcal curves.

information, the input sulcal curves contain many minor sulcal curves and extraneous curve segments, which should be refined. Our approach first chooses an example curve for each of the input major curves, if any, by adapting a spectral matching method (Leordeanu and Hebert, 2005) in computer vision to our problem setting, and then labels the input curve while also refining it with respect to the chosen example curve. We employ the spectral-based method since it is robust to noise and outliers and facilitates partial curve matching. Adopting a multi-resolution scheme for representing both the input and example curves, we are able to greatly reduce time and space complexities for the spectral matching. Refining an input sulcal curve involves three tasks: discarding minor input curves, cutting off extraneous branches of major sulcal curves, and filling small gaps between curve segments. Through experiments on the raw input sulcal curves automatically extracted from 30 subjects, we show the refining results are comparable in accuracy to those done manually.

Materials and method

Data acquisition

This study used the data set of the International Consortium for Brain Mapping (ICBM) (Mazziotta et al., 1995; Watkins et al., 2001). Data were collected from 152 unselected normal volunteers with written informed consents, under the approval of the Research Ethics Committee of the Montreal Neurological Institute and Hospital. The subjects were scanned using a Phillips Gyroscan 1.5 T superconducting magnet system which yielded a sequence of T1-weighted images (3-dimensional [3D] fast field echo scan with 140–160 slices, 1-mm isotropic resolution, time repetition [TR] = 18 ms, time echo [TE] = 10 ms, flip angle = 30). We collected a group of 148 subjects composed of 83 men and 65 women. Their ages ranged from 18 to 44 years (mean ± standard deviation: 25.0 ± 4.9 years). From this group, we selected 30 subjects for expert-provided example data acquisition, consisting of 15 men (26.8 ± 4.9 years) and 15 women (26.2 ± 4.0 years).

Input images were processed using the standard MNI anatomical pipeline without atlas-based surface registration. Using a linear transformation, the native MR images were first normalized into a standardized stereotaxic space and then corrected for intensity nonuniformity (Collins et al., 1994; Sled et al., 1998). The registered and corrected images were then classified into white and gray matters, the cerebrospinal fluid, and the background using an advanced neural-net classifier (Zijdenbos et al., 1996). Finally, the CLASP algorithm (Kim et al., 2005; MacDonald et al., 2000) was used to automatically extract the hemispheric surfaces of the inner and outer cortices with 40,962 vertices. The accuracy of this technique was recently demonstrated in a phantom-based quantitative cross-validation study, which showed the high geometric and topologic accuracy of the cortical surfaces (Lee et al., 2006). We used outer cortical surfaces for both extraction of the input sulcal curves and the expert-provided examples.

Automatic labeling and refining of major sulcal curves

Basic Idea

Let P and Q be a set of input sulcal curves on a cortical surface and a collection of expert-provided example data, respectively. Being extracted based on pure geometric information, P contains minor sulcal curves and major sulcal curves with extraneous branches.

In order to account for high variability of sulcal folding patterns, multiple example data are sampled from different subjects for each major sulcus. We used 24 (possibly disconnected) major sulcal curves per subject and 30 subjects to form example data. Thus, an example set Q provides the label of an input major sulcal curve and its geometric variations, which are to be used for labeling and refining an input major sulcal curve. We assume that every curve in P and Q is represented as a set of feature points on it.

Given P and Q, our objective is to label the major sulcal curves in P while pruning their extraneous branches and also removing the others from P, by following the neuroanatomical conventions conveyed by Q (Fig. 2). In order to achieve this goal, the most similar curve in P is chosen for each example data set in Q by spectral matching (Leordeanu and Hebert, 2005). Being regarded as a major curve, every chosen input curve receives the corresponding label of the example data set. The remaining curves in P are regarded as minor curves and thus discarded. The labeled input curve is also refined by cutting off its extraneous branches by referring to the example curve that is most similar among all curves in the set. Since an input major curve in P shares its label with the curves in the corresponding example set, there is a one-to-one correspondence between the major curves in P and the example data sets in Q. We further incorporate a simple multi-resolution scheme for curve representation to accelerate curve matching. Fig. 3 shows three different sets of sulcal curves: the

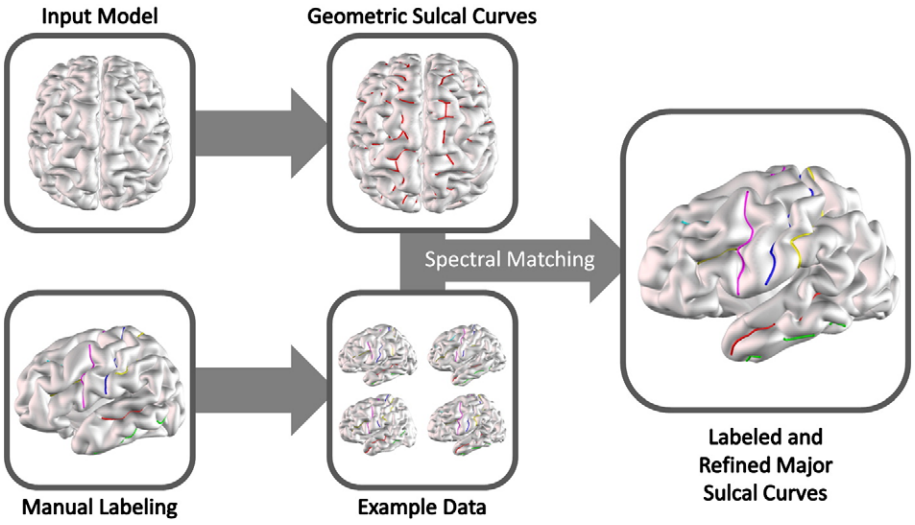

Fig. 2. Overview of the proposed approach: The input sulcal curves are extracted from a cortical surface using the automated algorithm. The input sulcal curves are then automatically labeled based on the expert-provided example data using the proposed spectral-based method. The results are the automatically labeled major sulcal curves on the cortical surface.

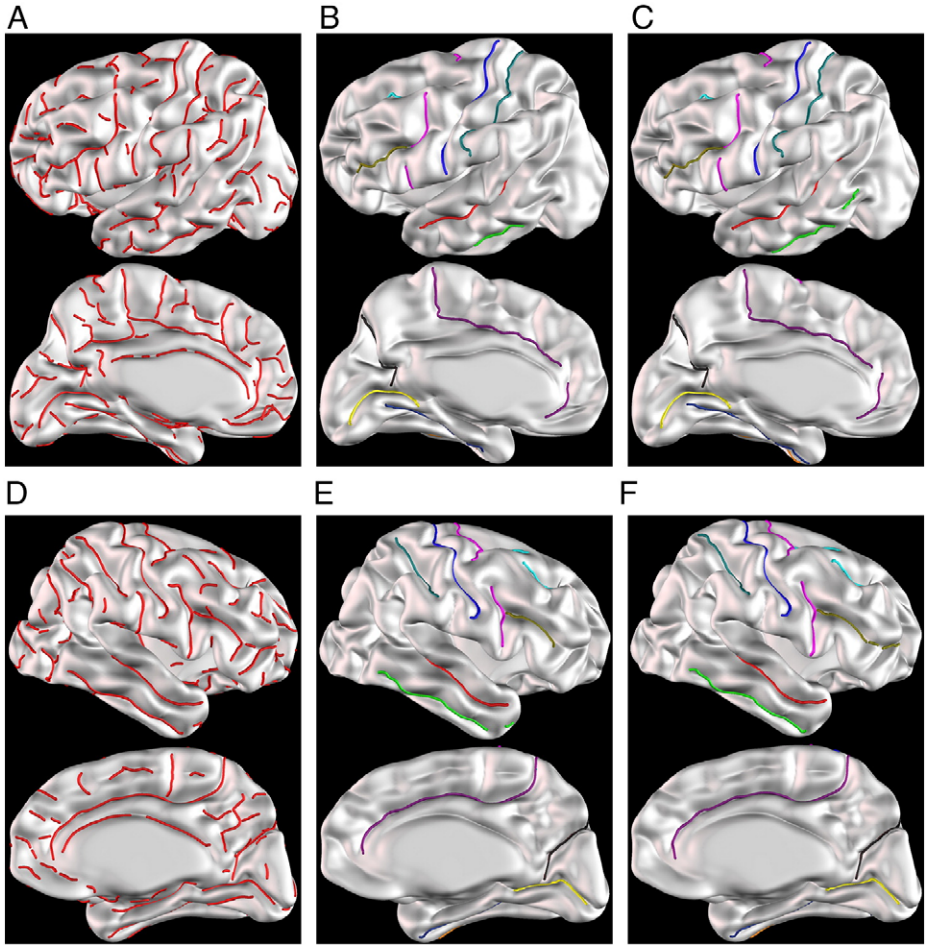

Fig. 3. Sulcal curves for left and right hemispheres of a cortical surface: the input sulcal curve set P (left column), the output major sulcal curves (middle column), and the corresponding ground truth sulcal curves (right column). The upper rows show the sulcal curves in the left hemisphere, while the lower rows exhibit those in the right hemisphere.

input sulcal curve set P (left column), the resulting output major sulcal curves (middle column), and the corresponding ground truth sulcal curves (right column). The top and bottom rows exhibit sulcal curves in the lateral and medial regions, respectively.

Spectral-based method

In order to find the most similar input sulcal curve in P to each example data set E in Q, we measure the similarity between every pair of curves which are from P and E, respectively. The pair with the highest similarity gives the input curve and its corresponding example sulcal curve in E. We assign the label of the example data set E to the input curve while simultaneously refining it using this example curve. We adapt a spectral matching technique in computer vision to measure the similarity between an input-example curve pair (Leordeanu and Hebert, 2005). Given a pair of curves (p,q) for $p \in P$ and $q \in E$, we estimate their similarity by exploiting the feature points of these curves and their relationship. Specifically, let p and q be represented by n and m feature points as follows:

$$p = \{p_1, p_2, \cdots, p_n\} \text{ and } q = \{q_1, q_2, \cdots, q_m\}. \tag{1}$$

For matching two sets of feature points, one could employ methods such as an iterative closest point (ICP) method (Besl and McKay, 1992) or a bi-partite graph matching scheme (Cormen et al., 2001). The ICP method finds correspondences between two sets of feature points assuming that there is a one-to-one correspondence between them. Since the ICP method iteratively searches for a local optimum based on the individual feature similarity, it is difficult to reflect the global shape of the sulcal curves and thus sensitive to noise and outliers (Chui and Rangarajan, 2003). Similarly, the bi-partite graph matching scheme exploits only the similarity between individual feature points, and thus it is sensitive to noise and outliers, too. The spectral matching method exploits the feature points themselves and their relationship as well. Consequently, this method is not only robust to noise and outliers but also facilitates partial matching between two sets of feature points.

The affinity of an assignment between two feature points (p_i,q_j) measures how well feature point p_i in p matches q_j in q. Letting $a = (p_i, q_j)$ and $b = (p_k,q_l)$ be two distinct assignments, the affinity between two assignments a and b measures how compatible two pairs of feature points, (p_i,q_k) in p and (q_j,q_l) in q, are with each other. We construct a matrix M to store the affinities of individual assignments and their pairwise affinities, where

$$M(a,b) = \begin{cases} \text{the affinity of } a, & \text{if } a = b \\ \text{the affinity of } (a,b), & \text{otherwise} \end{cases} \tag{2}$$

We set all affinity values to be nonnegative. As p and q have n and m feature points, respectively, there are nm assignments. Therefore, we have $nm \times nm$ pairs of assignments, of which the affinity values are stored in the $nm \times nm$ affinity matrix M.

We describe how to compute the affinity value for a pair of feature points. The major sulcal curves on a human cortical surface are characterized well by their geometry. We use geometric features to measure both the individual affinity $M(a,a)$ and the pairwise affinity $M(a,b)$, $a \neq b$. As all brain volumes were scanned in a common

stereotaxic coordinate system, geometric information is consistent across the subjects. In particular, a sulcus is found in a similar region of each cortical surface. As suggested in (Leordeanu and Hebert, 2005), we filter out the assignments that are unlikely to be correct. Specifically, an assignment $a=(p_i,q_j)$ is rejected if the distance between two feature points p_i and q_j is greater than a given threshold R. Each such rejection reduces the number of rows and that of columns by one. We set R to 1/6 of the radius of the minimum bounding sphere of the largest cortex model over all input and example ones.

We measure an individual affinity $M(a,a)$ using four pieces of geometric information on feature points p_i and q_j: positions, sulcal depths, curvatures, and unit tangent vectors. We adopt a 3D Cartesian coordinate system to represent a point. The sulcal depth of a point measures Euclidean distance from the point to the nearest voxel on the cerebral hull volume (Im et al., 2008a,b). The curvature at a point on a sulcal curve is estimated by approximating the curve as a piecewise linear curve. The unit tangent vector is also estimated at the point along this curve. We collect the information on each feature point r into an 8D vector $F(r)$ as follows:

$$F(r) = (x_r, y_r, z_r, d_r, \kappa_r, \bar{x}_r, \bar{y}_r, \bar{z}_r), \tag{3}$$

where (x_r,y_r,z_r),d_r,κ_r, and $(\bar{x}_r,\bar{y}_r,\bar{z}_r)$ represent the position, sulcal depth, curvature, and tangent vector estimated at the feature point r. For an assignment $a=(p_i,q_j)$, we define the displacement vector $D(a)$ as follows:

$$D(a) = F(p_i) - F\left(q_j\right). \tag{4}$$

Each element of $D(a)$ is normalized with respect to its maximum value. Let W be a unit weight vector that gives the importance of every element in $D(a)$, where every element of W is nonnegative. Then, the individual affinity $M(a,a)$ is

$$M(a,a) = exp^{-\frac{1}{2}\frac{||D(a)||_W^2}{\sigma^2}}, \tag{5}$$

where $||D(a)||_W^2$ denotes the weighted norm of $D(a)$ with respect to the weight vector W, and σ is a user-provided regularization parameter.

In order to measure the pairwise affinity $M(a,b)$,$a\neq b$ for two distinct assignments, $a=(p_i,q_j)$ and $b=(p_k,q_l)$, we define the pairwise displacement vector $D(a,b)$ as follows:

$$D(a,b) = D_q - D_p, \tag{6}$$

where $D_p=F(p_k)-F(p_i)$ and $D_q=F(q_l)-F(q_j)$. Each element of $D(a,b)$ is also normalized with respect to its maximum value. Using $D(a,b)$, the pairwise affinity $M(a,b)$ is given as follows:

$$M(a,b) = exp^{-\frac{1}{2}\frac{||D(a,b)||_W^2}{\sigma^2}}. \tag{7}$$

As explained in Leordeanu and Hebert (2005), we set $M(a,b)=0$ if the two assignments a and b do not agree (e.g. $D(a,b)$ is too large) or if they are incompatible (e.g. $i=k$ and $j\neq l$). In our experiments, we empirically set

$$W = \left(\frac{0.75}{3}, \frac{0.75}{3}, \frac{0.75}{3}, 0.05, 0.15, \frac{0.05}{3}, \frac{0.05}{3}, \frac{0.05}{3}\right), \text{and} \tag{8}$$

$$\sigma = 0.3.$$

A total weight of 0.75 is assigned to the first three elements of $D(a)$ or $D(a,b)$, 0.05 and 0.15 to the fourth and the fifth elements, respectively, and a total of 0.15 to the last three elements when evaluating Eqs. (5) and (7). By the way in which we build M, M is symmetric and nonnegative.

The affinity matrix M is used to choose a subset of consistent assignments, referred to as C, to measure the similarity between two curves, p and q. Based on the Raleigh ratio theorem, this subset is built guided by the principal eigenvector of M while enforcing the one-to-one correspondence constraint for the chosen assignments. Each element of the eigenvector gives the confidence of the corresponding assignment between a pair of feature points. Let L be the set of all input-example feature point pairs from curves, p and q. We choose the pair (p_i,q_j) with the maximum confidence from L as a consistent assignment in C. This pair together with all conflicting pairs with this pair is removed from L. Each conflicting pair contains either p_i or q_j as its element. For the remaining pairs in L, we repeat this process to construct the consistent assignment set C until either L becomes empty or the maximum confidence value for the remaining element in L is zero. We postprocess the subset C to filter out the assignments with low confidence values by thresholding. Appendix A presents an example of constructing the affinity matrix using two simple curves p and q.

Given the consistent assignment set C between curves p and q, their similarity A is computed by

$$A = \sum_{a,b\in C} M(a,b). \tag{9}$$

For every example data set in Q, the most similar curve in P is chosen in a greedy manner using the similarity value A. To do it, the spectral matching method selects the most similar curve in P to each curve in an example set E. Since E consists of 30 curves each of which is from different subjects, 30 input-example curve pairs are obtained. Among these pairs, our method chooses the pair with the highest similarity value to establish a correspondence between the selected input curves in P and the example data sets in Q. This correspondence is used to identify and label the major curves in P while discarding the others. The set C of consistent assignments for curves p and q provides the subset of feature points in an input curve p that best matches to that in an example curve q guided by the principal eigenvector of M. Thus, for the input-example curve pair (p,q), the extraneous branches of p are pruned by discarding the feature points that do not form any consistent assignments together with those in q. In theory, this greedy strategy does not always guarantee a one-to-one correspondence between the major curves in P and the example data sets in Q. For example, an input major curve may correspond to two or more example data sets and vice versa, even though neither was observed in practice. One may instead adopt a matching algorithm in graph theory (Dickinson et al., 2001) to guarantee the one-to-one correspondence after computing the similarity values for all input-example curve pairs, which imposes a heavy computational overhead. For efficiency, we took the simple greedy strategy in our experiments as described above.

Multi-resolution extension

An affinity matrix M is a sparse matrix, which is symmetric and positive. The dimension of M is $mn\times mn$, where n and m are the number of feature points in an input sulcal curve p in P and that in a sulcal curve q in an example data set E of Q, respectively. As $n\geq 10^2$ and $m\geq 10^2$ on average, the dimension of M is more than $10^4\times 10^4$. Although M is a sparse matrix, spectral analysis on this matrix is computationally demanding because of its high dimensionality. We present a multi-resolution framework for spectral analysis to filter out input-example curve pairs with low similarities at its early stages.

A sulcal curve on a cortical surface is composed of a collection of line segments, each of which has a sequence of feature points sampled from it. An input sulcal curve p in P has possible extraneous branches that are connected to the primary curve at junction points (Seong et al., 2010). Together with the primary

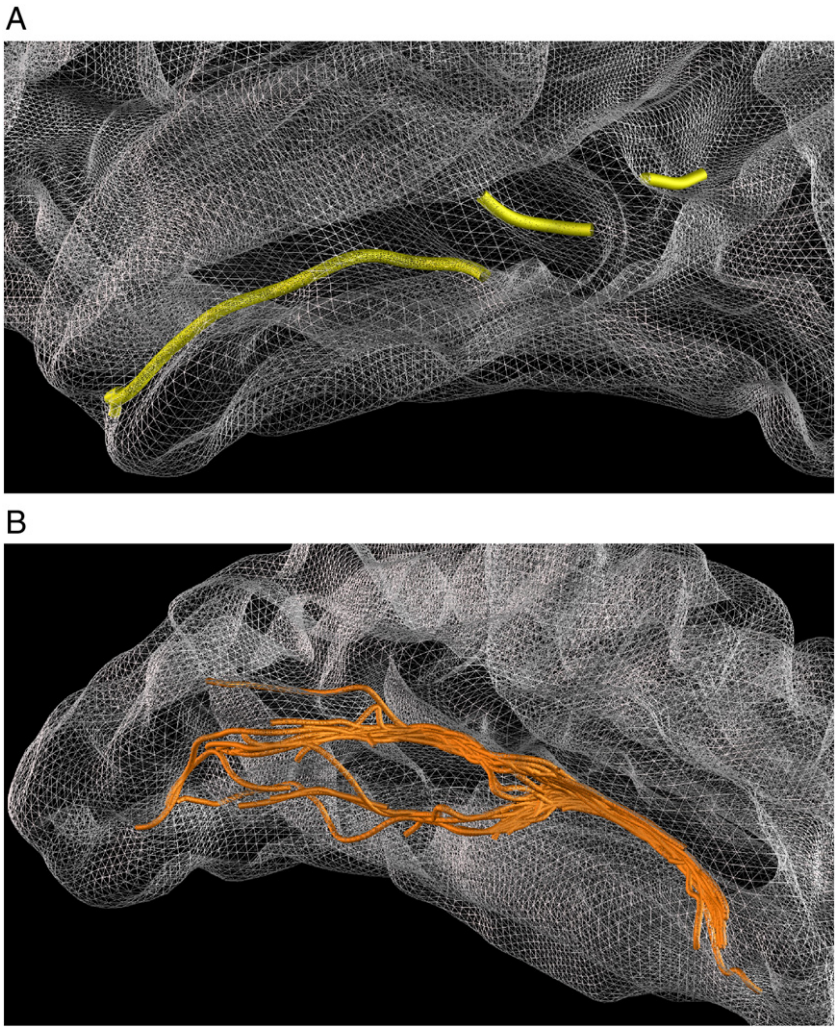

Fig. 4. ITS and LTOS show high variability: Each ground truth curve in the ITS is composed of multiple curve segments (A). The ground truth curves themselves in the LTOS are classified into two groups of curves with different shapes (B).

curve those line segments are represented using a tree from which a set of feature points is sampled. An example sulcal curve q in E is also represented as a tree with no branches from which a different set of features is sampled (Fig. 4).[1] The proposed spectral-based method finds the subset of feature points on the input curve p that best matches to that on the example curve q as explained in Spectral-based method. That is, our method facilitates partial matching between the two sets of feature points. Since input-example feature point correspondences are established regardless of the connectivity of curves p and q, our method can handle possibly disconnected sulcal curves. A feature point p_i on p is identified to be on a major sulcal curve if there is the corresponding feature point q_j on q such that (p_i,q_j) is a consistent assignment in C. We employ a curvature-adaptive scheme to sample a set of feature points of a curve. That is, more points are sampled from a higher curvature curve segment. The normal curvature along the curve is used for adaptive sampling. A finite difference technique is used to estimate the curvature assuming that the cortical surface is modeled as a triangular mesh (Rusinkiewicz, 2004).

[1] As exceptional cases the major sulcal curves in the ITS and the PreCS may be composed of a few disjoint curve segments. Fig. 4 shows an example of the ITS. By interpreting a gap between curve segments as a long interval with no feature points, even these exceptional curves can be represented as trees with no branches.

Every curve p in P is sampled adaptively to its curvature to form a feature point set p^0. This set is downsampled in a hierarchical manner to form a multi-resolution representation of p denoted by $(p^0,p^1,\cdots,p^s)$, where $p^r, 0 \le r \le s$ becomes successively coarser as r increases. Each example curve in E is also represented as a hierarchy of feature points $(q^0,q^1,\cdots,q^s)$ in the same fashion. Given the multi-resolution representation for all curves in P and E, the spectral analysis is performed level by level from the coarsest level s to the finest level 0. At level s, the number of input-example curve pairs is large, but the number of feature points in each set is small to result in the affinity matrix M of low dimensionality. Thus, the spectral analysis is done very efficiently, even though the number of input-example curve pairs is large. For each input-example curve pair (p,q), we build its consistent assignment set C to compute the similarity A at level s using Eq. (9). Curve pairs with low similarity values are discarded so that they are not considered at the next levels as long as each subset E has at least one example curve to form an input-example pair with an input curve in P. The same process is applied to each input-example pair of feature point sets, (p^{s-1},q^{s-1}) at the next finer level $s-1$. Although these sets become denser than their respective sets at the previous level s, the number of input-example curve pairs is greatly reduced, which still makes the spectral analysis at this level efficient. This iterative process is repeated to eventually perform the spectral analysis at the finest level 0 with a small number of input-example curve pairs. In our experiments, we set the number of levels in the hierarchy to 4, that is,

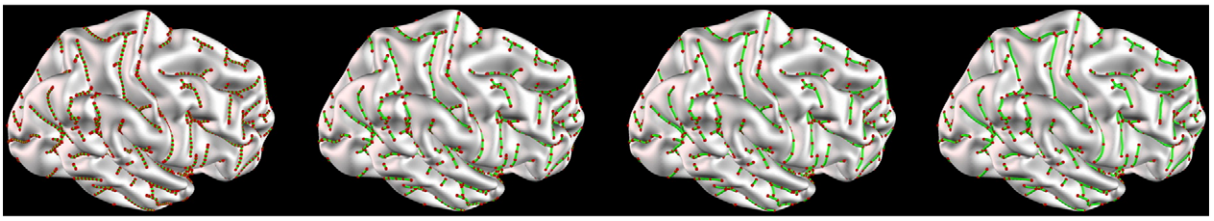

Fig. 5. Four levels of a multi-resolution representation: feature points (red spheres) are adaptively sampled from the sulcal curves (green curves) on the input model.

$s = 3$. As observed in Fig. 5, the number of feature points in each curve decreases greatly as the level of hierarchy increases.

Extracting sulcal curves from input cortical surface

A sulcal curve on a cortical surface is defined by a set of feature points that are located along high-curvature fundic regions within a sulcus. Seong et al. (2010) presented a geometric algorithm for extracting the sulcal curves on a human cortical surface using an anisotropic geodesic distance map. We briefly review this algorithm since an input sulcal curve is extracted by using it. The curve extraction algorithm consists of three steps: gyral region segmentation, anisotropic geodesic (AG) distance map construction, and sulcal curve extraction as illustrated in Fig. 6.

In order to segment gyral regions in the cortical surface Ω, we measured the sulcal depth at each point in Ω, which is the Euclidean distance from the vertex to the nearest voxel on the cerebral hull volume (Im et al., 2008a,b). A vertex in Ω is regarded to be in a gyral region if its depth is shallower than a threshold. In our study, we used 4.5 mm as a threshold. The segmented gyral regions are colored blue in Fig. 6(A).

Given a set of gyral regions G, we compute the sulcal regions by complementing them with respect to the cortical surface Ω. Then, the problem of computing the AG distance map can be reduced to that of solving an anisotropic front propagation equation

$$\begin{aligned} &||\nabla u(\mathbf{x})||F\left(\mathbf{x}, \frac{\nabla u(\mathbf{x})}{||\nabla u(\mathbf{x})||}\right) = 1, \quad \mathbf{x} \in \Omega\, G \\ &u(\mathbf{x}) = 0, \qquad\qquad\qquad\quad \mathbf{x} \in G \end{aligned} \tag{10}$$

where F is a speed function (Jackowski et al., 2005). We used a quadratic (bilinear) speed function

$$F\left(\mathbf{x}, \frac{\nabla u(\mathbf{x})}{||\nabla u(\mathbf{x})||}\right) = \frac{\nabla u(\mathbf{x})^T}{||\nabla u(\mathbf{x})||} M(\mathbf{x}) \frac{\nabla u(\mathbf{x})}{||\nabla u(\mathbf{x})||}, \tag{11}$$

where a tensor matrix $M(\mathbf{x})$ is designed in an application-dependent manner. An AG map contains the minimum arrival time $u(\mathbf{x})$ of the front to every vertex $\mathbf{x}$ on the surface from the gyral points. $\mathbf{M}(\mathbf{x})$ is built based on the normal curvature of the cortical surface such that the front propagation speed F is high on a low curvature region, while being low on a high curvature region. Fig. 6(B) shows the AG map for a cortical surface. Red color represents "far from" the gyral regions, while blue does "close to" them.

With the AG map constructed, we first take the complement of the gyral regions G with respect to the cortical surface Ω to identify the sulcal regions $S = \Omega \backslash G$. A sulcal region may consist of two or more disconnected subregions. Thus, a sulcal curve consists of (possibly disconnected) curve segments, each of which is the skeleton of a subregion and represented by the set of points on the skeleton:

$$\begin{aligned} SC = \{&w \in \Omega \,|\, \exists w_1, w_2 \in \mathcal{B}(S) \text{such that } AGDist(w, w_1) \\ &= AGDist(w, w_2), w_1 \neq w_2\}, \end{aligned} \tag{12}$$

where AGDist(u,w) denotes the AG distance between two points u and w on the surface, and $B(S)$ is the boundaries of sulcal regions $S = \Omega \backslash G$. The points in SC can be traced guided by the radial flow over the skeleton (Damon, 2005). The feature points of a sulcal curve segment are sampled to represent the curve segment as a piecewise linear curve. Fig. 6(C) shows the resulting sulcal curves.

Expert-provided example sulcal curves

A collection of expert-provided example data sets was obtained from automatically extracted sulcal curves by manually editing and labeling these according to neuroanatomic conventions. For expert-provided example data acquisition, we used 30 ICBM surface data which consist of 15 men and 15 women (Data acquisition).

We adopt the sulcal curve-based scheme to represent cortical sulci (Fillard et al., 2007). Sulcal curves lie in high-curvature fundic regions of the cortical surface to divide the surface into gyral regions as shown in a classical cytoarchitectonic map of Brodmann. It is time-consuming to manually trace a sulcal curve that follows high curvature fundic regions of a sulcus. For efficiency, we used the recent method in Seong et al. (2010) to automatically extract the initial sulcal curves that trace valleys of the sulcal regions. The automatically extracted sulcal curves were edited by experts based on the neuroanatomical protocol in order

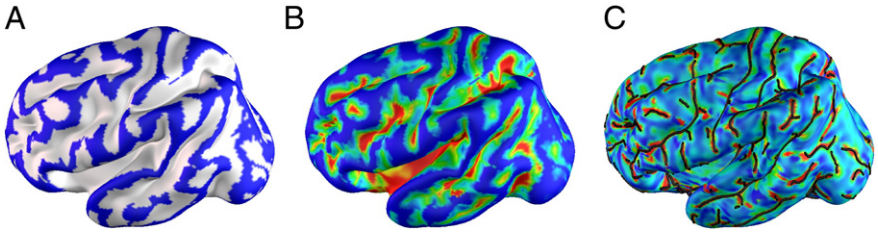

Fig. 6. A pipeline for extracting geometric sulcal curves from human cortical surface: the gyral region segmentation (A), the anisotropic geodesic (AG) distance map construction (B), and the sulcal curve extraction (C).

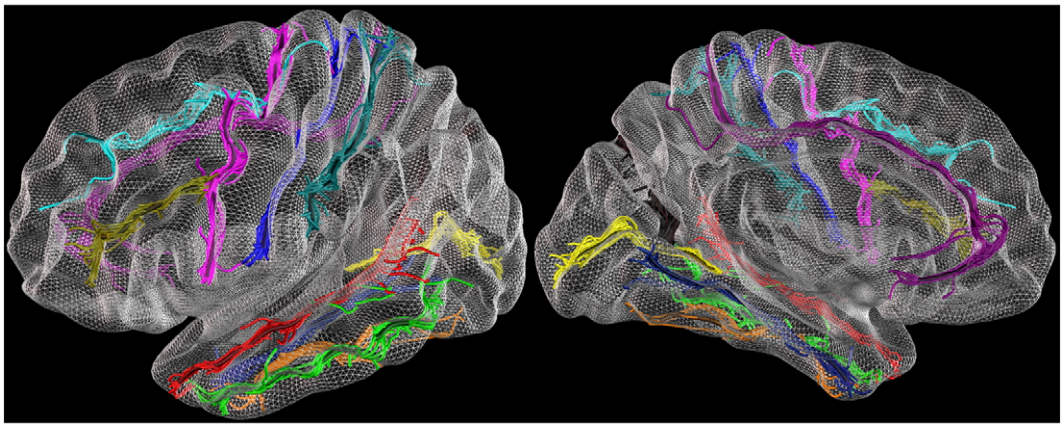

Fig. 7. Sulcus variability of a manually labeled example set: the bold curves among sulcal bundles indicate the mean curves. A set of the ground truth curves in each sulcus is acquired from 30 subjects and visualized on the atlas cortical surface. Since the sulcal curves for each individual subject are mapped onto the atlas model, they may not follow the high curvature fundic regions on the atlas surface.

to provide a set of accurate major sulcal curves for the example data collection.

Given the automatically extracted sulcal curves from the cortical surfaces of 30 subjects, an interactive drawing/editing tool in a surface modeling system was used to manually label and refine these curves to obtain a set of example sulcal curves. Four neuroanatomists who were blind on subject sex and age traced and edited the sulcal curves interactively on the lateral brain surface (including superior temporal sulcus (STS), inferior temporal sulcus (ITS), central sulcus (CS), precentral sulcus (PreCS), superior frontal sulcus (SFS), inferior frontal sulcus (IFS), postcentral sulcus (PostCS), and lateral temporo-occipital sulcus (LTOS)) in each hemisphere of a cortex model (see Appendix B for more details on each sulcus). An additional set of sulcal curves was also labeled manually on the medial surface (including medial temporo-occipital sulcus (MTOS), cingulate sulcus (CingS), calcarine fissure (CalcF), and occipito-parietal sulcus (OPS)). The resulting example sulcal curves were validated by the department of neurology at Samsung Medical Center, Korea. The example data set consists of a total of 24 types of sulcal curves since they consistently appeared in all 30 normal subjects. Each of these types gives rise to an example data set with the same label.

Fig. 1 shows both lateral and medial regions of five left hemispheres with manually labeled major sulcal curves. We used an inflated surface model for better visualization. In our experiments, original outer cortical surfaces were employed for both

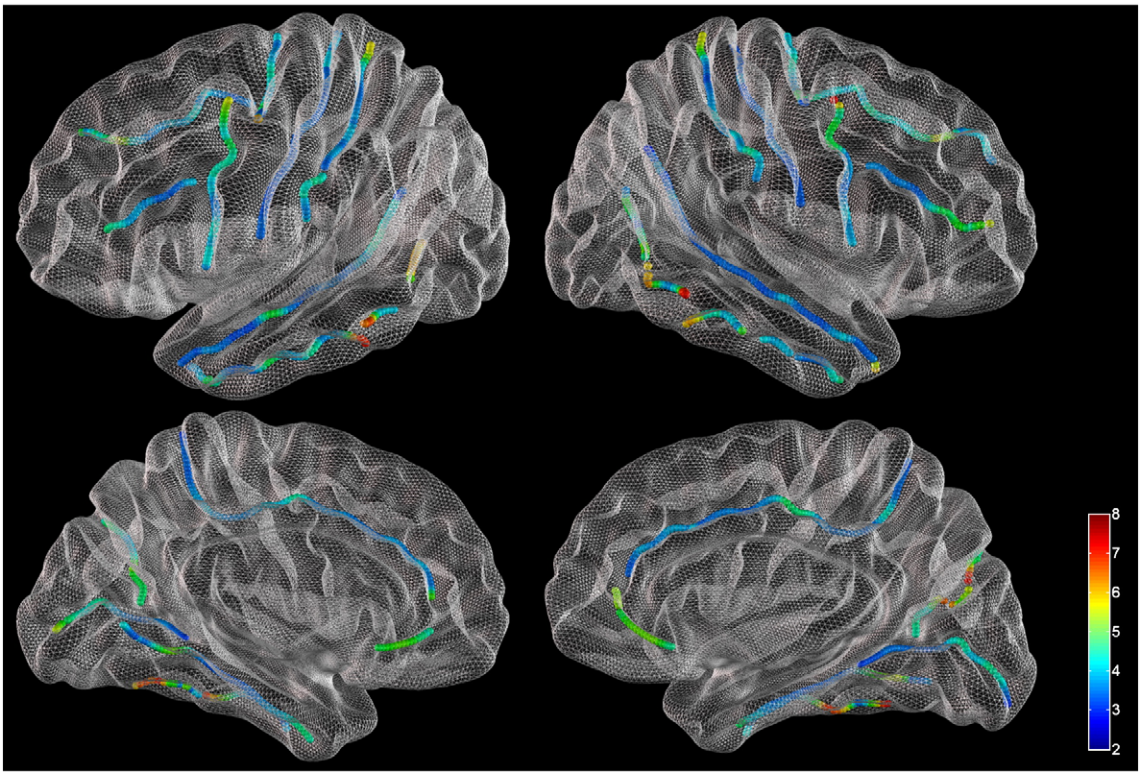

Fig. 8. Variability maps of manually labeled sulcal curves in lateral (upper row) and medial (bottom row) regions: The highest value of variability (red) on the color map is more than 8, and the lowest value (blue) is less than 2 in the RMS measurement. Note that sulcal curves have high variability at their extremes.

Table 1
The variability data of the ground truth curves for each sulcus.

Sulcus		STS	ITS	CS	PreCS	PostCS	SFS
	Left	1.87 ± 0.80	2.75 ± 1.93	1.93 ± 0.30	2.59 ± 0.82	2.37 ± 0.80	2.40 ± 0.75
Avg. Var.	Right	1.99 ± 0.55	2.95 ± 1.63	1.86 ± 0.27	2.48 ± 0.90	2.38 ± 0.77	2.64 ± 0.74
Sulcus		IFS	LTOS	MTOS	CingS	CalcF	OPS
	Left	2.13 ± 0.54	3.52 ± 1.85	2.33 ± 0.68	2.28 ± 0.57	2.35 ± 0.77	2.82 ± 0.74
Avg. Var.	Right	2.51 ± 0.84	3.40 ± 1.90	2.46 ± 0.93	2.46 ± 0.79	2.11 ± 0.45	3.74 ± 1.49

Given the ground truth curves in the example data set, the variability of each feature point sampled from the ground truth curve was measured using the squared root of the trace of the covariance matrix that was estimated at the point using Eq. (16). This table presents the average and standard deviation of the variability for each sulcal curve.
Data: mean ± SD (range); unit: mm.

automatically extracting the sulcal curves and manually labeling major sulcal curves.

Variability analysis

Sulcus variability analysis

The accuracy of the proposed method depends greatly on the expert-provided example data. Even with extensive studies on variability analysis of sulcal folding patterns in human brains (Ochiai et al., 2004; Dubois et al., 2008; Cachia et al., 2008; Perrot et al., 2008), it is still nontrivial to determine the degrees of freedom for representing a sulcal shape. In this work, we used the example data to represent the variability of every sulcus by collecting the human brains of 30 normal subjects. We first describe how to analyze the variability of the example sulcal curves and then show the results on variability analysis.

Given a collection Q of expert-provided example data sets, we analyze the variability of the example sulcal curves in each set. The quantitative comparison of brain architectures across various subjects requires a common coordinate system to consistently represent their spatial features (Evans et al., 1996). To identify the corresponding regions between subjects, the individual surfaces were aligned to the surface group template (standard atlas model) based on 2-D surface-based registration. Note that the atlas-based registration technique was employed for sulcus variability analysis but not for spectral matching. The surface group template is unbiased and of high-resolution with enhanced anatomic details, being constructed by an iterative registration scheme from a group of 222 subjects' hemispheres (Lyttelton et al., 2007). The vertices of each surface were registered to the surface group template, and variable sulcal folding patterns were aligned through a sphere-to-sphere warping algorithm (Robbins et al., 2004; Lyttelton et al., 2007). The sulcal curves that were extracted from the aligned cortical surfaces were also mapped onto the group template. The sulcal curves were then represented as B-spline curves on the cortical surface using cubic basis functions by employing a chord length parameterization (Farin, 1988). The number of control points for each B-spline curve was set to one half of that of the feature points of the sulcal curve.

For variability analysis, we used the covariance matrix for the curves in each set. In order to compute this matrix, we start with describing how to obtain the mean curve of the set. As pointed out in (Fillard et al., 2007), it is difficult to fully characterize sulcal curves using local differential properties, due to their high variability across subjects. In general, these curves do not possess intrinsic shape characteristics that are consistent over subjects. Therefore we choose, as the mean curve m, the curve that minimizes the total variance of the sulcal curves from it. The total variance V is defined as follows:

$$V = \frac{1}{N-1}\sum_{i=1}^{N} \int_0^1 ||c^i(s) - m(s)^2||ds, \tag{13}$$

where N is the number of example sulcal curves (subjects) in the set, c^i is the example curve for subject i, and s is a curve parameter value. For efficiency, we approximate the total variance V by discretizing Eq. (13):

$$V = \frac{1}{N-1}\sum_{i=1}^{N}\sum_{j=1}^{K} ||c^i(s_j) - m(s_j)||2, \tag{14}$$

where $s_j j = 1,2,\cdots,K$, are sampled parameter values. We set $s_l = 0$ and $s_K = 1$ to represent the start and end points of the curve, respectively. The mean curve m is obtained by minimizing V with an iterative B-spline approximation technique (Farin, 1988).

Given the mean sulcal curve of each example data set that represents one of the 24 major sulcal curves, the covariance matrix $\Sigma(s_j)$ at parameter s_j is estimated as follows:

$$\Sigma(s_j) = \frac{1}{N-1}\sum_{i=1}^{N}\left[c^i(s_j) - m(s_j)\right]\left[c^i(s_j) - m(s_j)\right]^T, j = 1,2,\cdots,K, \tag{15}$$

where $[(c^i(s_j) - m(s_j))]$ is a 3D column vector. $\Sigma(s_j)$ determines the spatial variance of the feature points sampled at s_j from the sulcal curves in an example data set. Specifically, the squared root of the trace of each covariance matrix, that is, $\sqrt{\text{trace}(\Sigma(s_j))}$ measures the variability at the sampled point with parameter s_j (Fillard et al., 2007).

Fig. 1 shows both the lateral and medial regions of five left hemispheres in the ground truth example data collection. The sulcal variability is clearly observed even for five subjects in this figure. For example, the shape of the precentral sulcus (PreCS) varied largely in the second and fifth subjects. We estimated the variability of the ground truth sulcal curves for every sulcus: The mean sulcal curve for each sulcus was first computed using Eq. (14). Fig. 7 shows the mean curve for every sulcus together with the set of the ground truth curves for the sulcus acquired from 30 subjects, where the mean curve is marked in dark color. Only curve bundles in the left hemisphere are visualized since the similar results are obtained for the right hemisphere. We mapped the sulcal curves for each individual subject onto an atlas model for visualization. Given the mean curve for each sulcus, we estimated the covariance matrix using Eq. (15), from which the variability of each sampled point on the sulcal curve was computed as the squared root of the trace of the covariance matrix. In Fig. 8, color maps represent the variability of the curves for every sulcus along their mean curve. Blue and red colors depict regions with

Table 2
The intra- and inter-operator variability (OV) was estimated for expert-provided example sulcal curves using the FLE given in Eq. (16).

		Intra-OV (expert RJH)	Intra-OV (expert KMJ)	Inter-OV
1.5ex AverageFLE	Left	1.19 mm	0.79 mm	1.22 mm
	Right	1.05 mm	1.22 mm	1.48 mm

Two neuroanatomists manually extracted 24 major sulcal curves (12 for each of the left and right hemispheres) from 5 subjects that were randomly selected among 30 ICBM data sets. In this table, experts RJH and KMJ represent two neuroanatomists, Jee Hoon Roh and Min-Jeong Kim, respectively, who manually extracted 24 major sulcal curves.

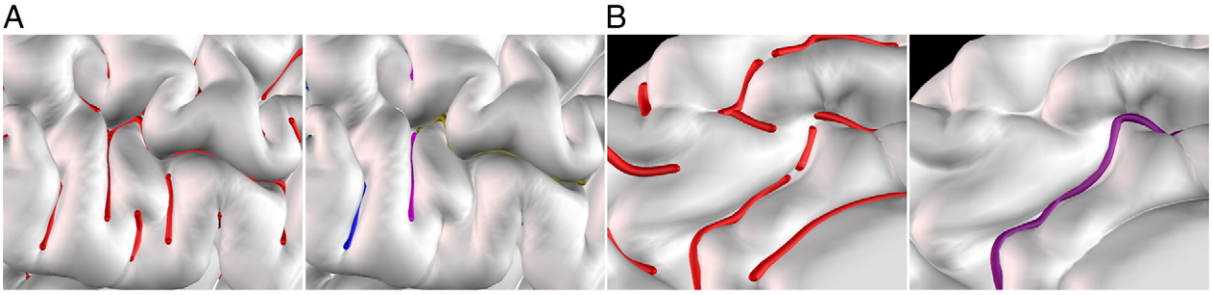

Fig. 9. The proposed automated method not only assigns neuroanatomical labels to the input sulcal curves but also refines those sulcal curves based on the user-provided example data: minor sulcal curves are discarded (A), and gaps between sulcal curve segments are filled in and extraneous parts of sulcal curves are cut off (B). Left figures in panels (A) and (B) show input sulcal curves and right ones represent the refined output curves.

low and high variability, respectively. In general, each curve shows a large variability at its extremes. The variability was measured at each sampled point on a sulcal curve. We computed the average and standard deviation of those variability values for the sulcal curve. Table 1 summarizes the variability data for each sulcus.

Operator variability analysis

In practice, the example sulcal curves may contain errors due to the variability of manual labeling. Therefore, we evaluated the variability among experts in manual marking of major sulcal curves using the fiducial localization error (FLE) given in Fitzpatrick et al. (1998) and Noblet et al. (2006). Suppose that a major sulcal curve was manually marked (delineated) N times. Then, every feature point $\mathbf{u}$ on the curve has N values $\mathbf{u}^i$, $i=1,2,\cdots,N$. Letting $\mathbf{u}^-$ be the mean of these values, the variability at point $\mathbf{u}$ is set to

$$\mathrm{FLE}(u) = \sqrt{\frac{1}{N-1}\sum_{i=1}^{N} ||\mathbf{u}^i - \overline{\mathbf{u}}||^2}. \quad (16)$$

In order to evaluate the variability of experts, two of them manually labeled 24 major sulcal curves twice (12 for each of the left and right hemispheres) for 5 subjects which were randomly selected among 30 ICBM data sets. Equivalently, each sulcal curve was labeled four times in total by them. Therefore, N was set to be two and four in Eq. (16) for intra- and inter-operator variability, respectively. Table 2 summarizes the average operator variability for the sulcal curves on the left and right hemispheres. The FLE measures the average deviation of manually marked sulcal feature points from their mean value for each feature point, which therefore represents the reliability of the manual marking. In Table 2, the intra-operator variability of expert KMJ is, for example, smaller than that of expert RJH for the left hemisphere, which implies that expert KMJ manually marked the sulcal curves in the left hemisphere in a more consistent manner. The inter-operator variability between the two experts measures how consistently they marked the sulcal curves with each other. With repeated training on test sets of cortical surfaces, the maximum allowed operator variability at every feature point was ensured to be less than the (inter-subject) variability given in Table 1 (Section 3.1).

Results

Given a cortical surface model, we first extracted input sulcal curves from a cortical surface using the automated method (Seong et al., 2010) outlined in Extracting sulcal curves from input cortical surface. Those input sulcal curves were then represented in a hierarchical manner by adaptively downsampling the feature points of each sulcal curve. A four level hierarchy was adopted for the multi-resolution representation of a curve. A collection of the expert-provided example data sets was acquired in ICBM data format from 30 cortical surfaces: 24 major sulcal curves were manually labeled for each cortical surface. The proposed spectral-based method in the Automatic labeling and refining of major sulcal curves section was then employed to identify and label the input major sulcal curves, while refining them according to the anatomical conventions conveyed by the example data sets.

Inspired by a jackknife/leave-one-out technique, we employed a similar technique to validate the accuracy of the proposed method: Each subject in turn was taken out of the set of subjects in order to automatically extract a set of input sulcal curves from the cortical surface of this subject. Accordingly, the expert-provided example curves for the subject were removed from the example data collection Q. The removed example curves were regarded as the ground truth sulcal curves for the subject. Unlike in a standard leave-one-out technique, we used as the input data the set of newly extracted sulcal curves rather than that of removed example curves. The input sulcal curves are thus different from those in the example data sets. The error of an output sulcal curve was estimated as the percentage of the length of the output curve with respect to that of the respective ground truth curve.

All experiments were performed on a PC equipped with an AMD Phenom(tm) II X4 905e 2.5 GHz CPU with 4.00 GB memory. For extracting input sulcal curves from a cortical surface, it took 36 min on average. The proposed spectral-based method took 17 min on average in automatically labeling and refining the input sulcal curves of a cortical surface. We implemented the proposed method using Matlab and we are planning to make the Matlab code publicly available.[2] We exploited the four level hierarchy for the multi-resolution representation of sulcal curve data. The multi-resolution framework effectively coped with the high dimensionality of the affinity matrix M.

The resulting major sulcal curves accurately traced high curvature fundic regions in sulci. The accuracy of the automatically refined sulcal curves was comparable to that of the manual labeled ones. Fig. 3 shows the sulcal curves for the left and right hemispheres of a cortex model. The upper and lower rows visualize the lateral and medial regions, respectively. The left columns and the middle columns in Fig. 3 exhibit the input sulcal curves and the output sulcal curves, respectively, while the right ones show the corresponding ground truth curves, which were labeled manually. As observed in this figure, the automatically refined curves (output curves) are indistinguishable from those of the corresponding ground truth curves. We used an inflated cortical surface model in order to better visualize the sulcal curves. The zoom-in views of a cortical surface in Fig. 9 show discarded minor curves (Fig. 9(A)), and filled-in gaps between curve segments of major sulcal curves and pruned extraneous curve segments (Fig. 9(B)). In Fig. 9(A) and (B), the left figures show the input sulcal curves and the right ones exhibit the resulting refined curves.

Fig. 10 depicts the deviation of output curves from their respective ground truth ones. We define two different types of errors: incomplete errors and false-positive errors. The former error results from an incomplete sulcal curve by incorrectly discarding a part of an input curve

[2] Please check http://cana.kaist.ac.kr/softwaredata/ for updates.

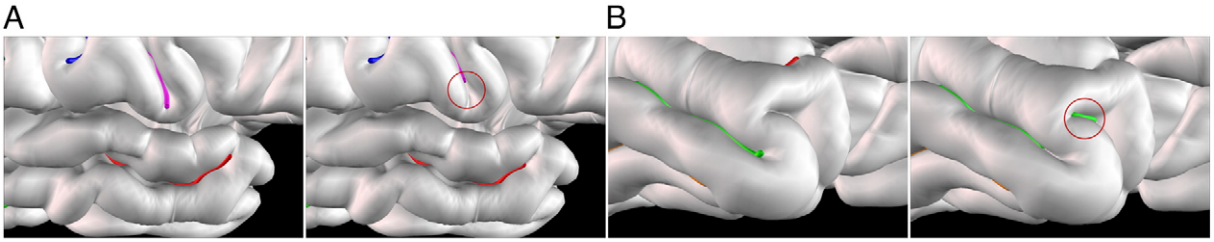

Fig. 10. Two different types of errors: incomplete errors (A) and false-positive errors (B). The former error results from an incomplete sulcal curve by incorrectly discarding a part of an input curve, and the latter comes from an under-refined curve by including an extraneous part of the input curve. In each figure, mis-matched parts are shown in red circles.

(Fig. 10(A)), and the latter comes from an under-refined curve by including an extraneous part of the input curve (Fig. 10(B)). In each of Fig. 10(A) and (B), the left figure gives a ground truth curve.

In order to visualize the error of each output curve, we estimated the mean of the sulcal curves in the corresponding example set of Q using Eq. (14) in Sulcus variability analysis. Every output curve was mapped to the corresponding mean curve by chord length parameterization and then the accuracy of the proposed method is visualized with a color map on an atlas model as shown in Fig. 11. Regions containing curves with low and high accuracy values are colored red and blue, respectively. Most output curves exhibited accuracy values higher than 80%, and the mean accuracy values of the curves in the left and right hemispheres were 84.69% and 84.58%, respectively. False positive errors were also lower than 8% for most output curves, and the mean false positive errors of the curves in the left and right hemispheres were 8.52% and 8.88%, respectively.

Fig. 12 summarizes accuracy statistics. The horizontal axis depicts accuracy ranges, while the vertical axis represents the percentage of the output sulcal curves. The left and right histograms in the top row show the accuracy statistics of the output curves in the left and right hemispheres, respectively, while those in the bottom rows give the cumulative statistics of the same data. As demonstrated in the histograms, nearly 70% of the output curves were refined with accuracy of better than 80%.

In Fig. 13, the accuracy of output curves is exhibited both for each sulcus and for each subject. The left and right columns present accuracy statistics for the left and right hemispheres, respectively. The histograms in the upper row show the accuracy and the false-positive error of output curves for each sulcus, and the plots in the lower row exhibit the same quantities for each subject. High accuracy was observed for most major sulcal curves. Specifically, accuracy of more than 90% was measured for the central sulcus (CS), the cingulate sulcus (CingS), and the calcarine fissure (CalcF) in the left hemisphere. In the right hemisphere, the similar accuracy was measured in the CS, the superior temporal sulcus (STS) and the CalcF. The error due to false-positive errors seemed to be inversely proportional to the accuracy of refinement. For example, false-positive errors were observed relatively frequently for the inferior temporal sulcus (ITS) and the superior frontal sulcus (SFS) in both hemispheres, where the accuracy was relatively low (58% and 79% on average, respectively). The average accuracy over all subjects was 84.64%. For most subjects, high accuracy values (more than

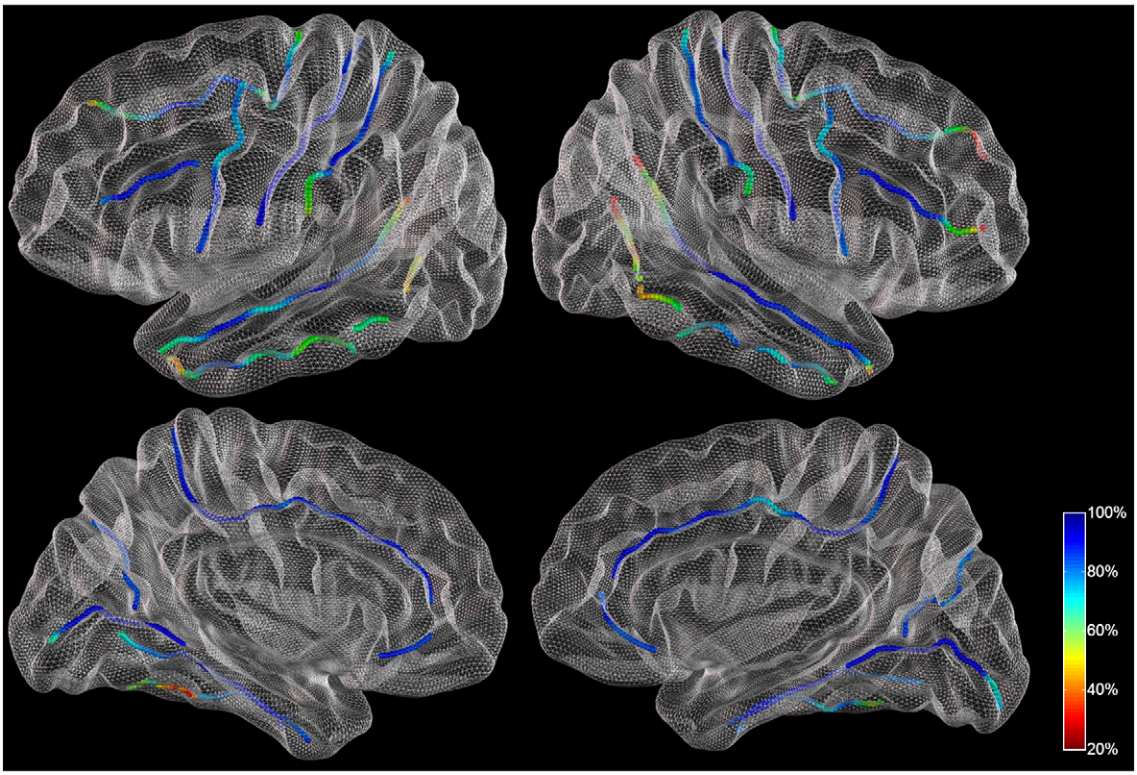

Fig. 11. Color map of the accuracy of the proposed labeling and refining method for the left and right hemispheres with lateral (upper row) and medial (bottom row) regions. Regions containing curves with low and high accuracy values are colored red and blue, respectively. The accuracy is low along a curve with high variability. For example, CS, CalcF, and OPS have many feature points with high accuracy, while ITS has points with relatively low accuracy.

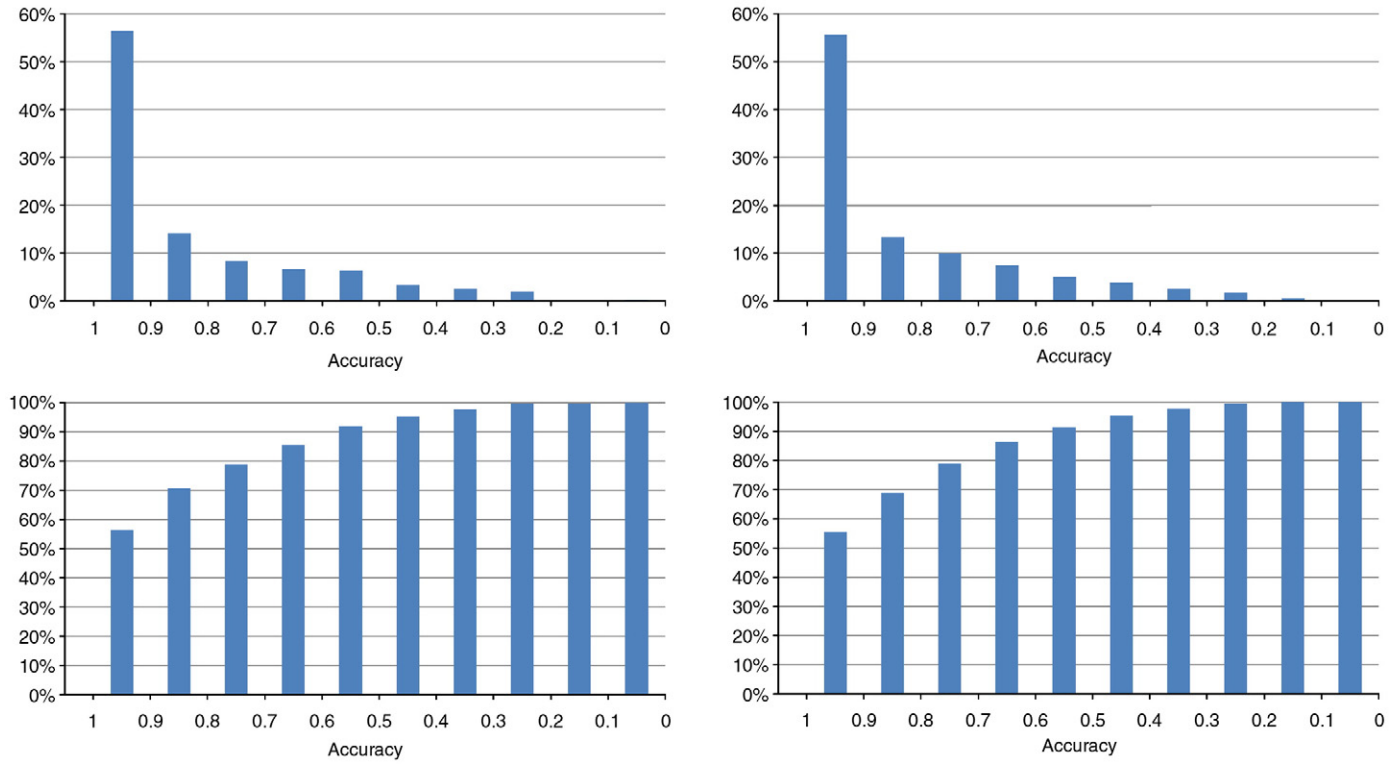

Fig. 12. Accuracy histograms: Top row: accuracy histograms for the left and right hemispheres. Bottom row: cumulative histograms for the same data. The horizontal axis depicts accuracy ranges, while the vertical axis represents the percentage of the output sulcal curves.

80%) and low false-positive errors (less than 8%) were observed. Two subjects showed relatively low average accuracy values (near 75%) and relatively high false-positive errors (slightly more than 15%).

We finally compared the lengths of identically labeled output curves with those of their respective ground truth curves. For this purpose, we estimated the mean length and standard length deviation of the output curves for every sulcus as well as those of the ground truth curves. As illustrated in Fig. 14, the differences of these statistics between the output and ground truth curves for each sulcus were not significantly large from a statistical standpoint. The contribution to the length of each sulcal curve due to the false-positive error is marked red on the top of the respective bar.

In general, our method correctly labels the input sulcal curves while refining them as illustrated in Fig. 12. The accuracy of the proposed

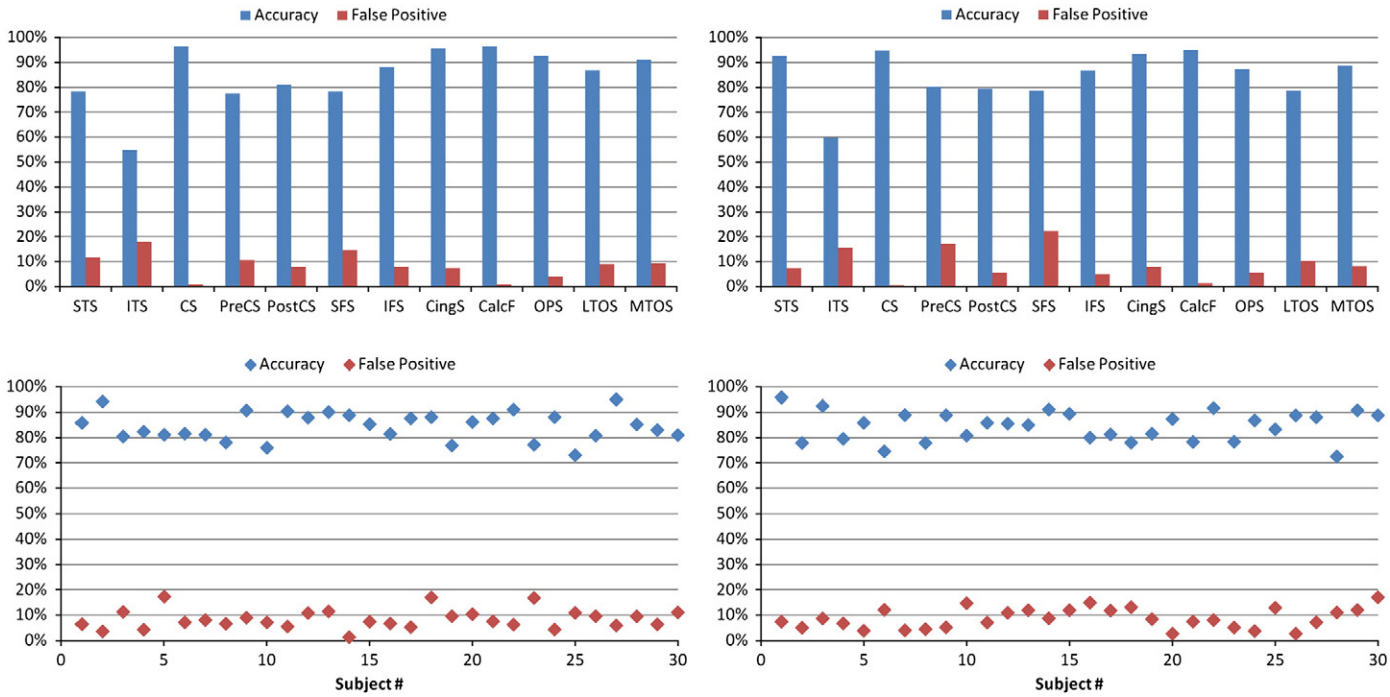

Fig. 13. Accuracy histograms: Top row: accuracy and false-positive error histograms for each sulcus. Bottom row: accuracy and false-positive error plots for each subject. Left and right figures correspond to left and right hemispheres, respectively.

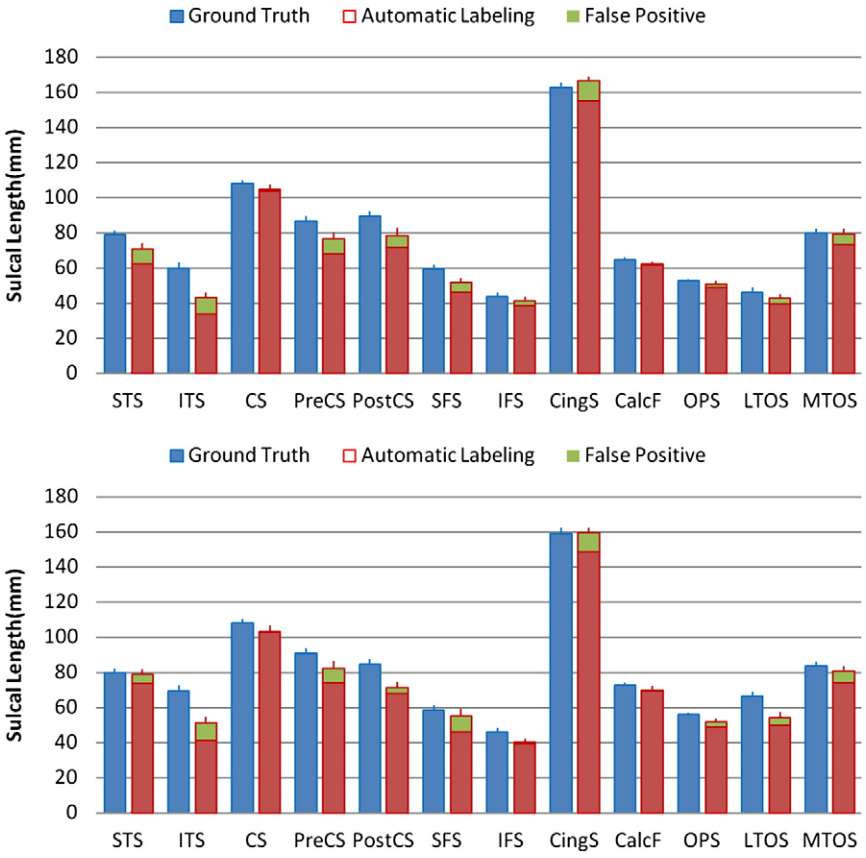

Fig. 14. Comparison of length statistics for 12 major sulcal curves across 30 subjects. Top and bottom figures correspond to left and right hemispheres, respectively.

spectral-based method depends on the expert-provided example data. In fact, our method works well as long as there exists a sulcal curve in the example data that is sufficiently similar to each input major sulcal curve. This could be achieved by increasing the population of the user-provided example sulcal curves. That is, a large number of example curves are likely to increase the accuracy for sulcal curves with high variability under the assumption that the example curves are correct.

Discussion

As demonstrated in the previous section, the automatically labeled and refined sulcal curves by our method were similar to their respective ground truth ones that traced the high-curvature fundic regions along their valleys within a sulcus. Fig. 3 shows examples of the output sulcal curves on a cortical surface. Human cortical sulci have complex folding patterns in brain cortices. Cortical sulci could be defined differently depending on applications. It is, however, critical to find their steady patterns in neuroimaging studies. The cortical sulci can be divided into three groups according to their appearance order during brain development: the primary, secondary, and tertiary sulci. The primary sulci appear during the early stage of brain development, in which the variability is thus low over population (Riviere et al., 2002; Regis et al., 2005; Perrot et al., 2008). Previous quantitative studies on intersubject variations revealed that sulcal patterns are more consistent and invariant in sulcal fundic regions, being more strongly predetermined during brain development (Lohmann et al., 1999, 2008). It has been conjectured that the deepest parts of sulci may not only be ontogenetically important but also related to brain functions (Hasnain et al., 2001). The sulcal curves along these parts could provide diagnostic data in discovering brain diseases (Cachia et al., 2008; Seong et al., 2010). These sulcal curves can also be used to analyze structural variability of sulci across different brains.

The proposed labeling method identifies the major sulcal curves from the input sulcal curves in a human cerebral cortex while refining them. Extracted from the cortical surface based on pure geometric data, the input sulcal curves may contain small branches or short curve segments along local valleys near the sulcal regions. Compared to the primary sulci, both the secondary and tertiary sulci are formed at the later stages of brain development by sulcal convolution, which causes the presence of small folds or branches around major sulci. These folds and branches vary in numbers and locations across different individual brains. Therefore, discarding minor sulcal curves and pruning extraneous branches may be useful in neuroimaging applications. Our approach to automated refining of sulcal curves performs this task by exploiting the collection of expert-provided example data sets, each composed of only major sulcal curves with an identical label. As shown in Fig. 9, our method can identify and label the primary sulcal curves, while removing extraneous minor curves and branches.

The accuracy of our method is correlated to the variability of the ground truth sulcal curves in every sulcus. For example, low variability was observed for the STS and the CS in the lateral region as well as the CingS and the CalcF in the medial region (Table 1). The ground truth curves in each of those sulci are consistent, being similar in shape across the subjects. On the other hand, relatively high variability was observed in the ITS in the lateral region compared to the others. Unlike the ground truth curves in sulci such as the STS, the CS, the CingS and the CalcF, the ground truth curves in the ITS were not consistent. Most of these curves were composed of multiple curve segments which were inconsistent in their shapes across the subjects (Fig. 4(A)). Exceptionally, high accuracy was observed in some sulcal curves with high variability such as the LTOS in the lateral region and the OPS in the medial region. The example curves in the LTOS were classified into two groups of curves with different shapes (Fig. 4(B)). However, even with their high variability, a similar example sulcal curve to an input LTOS curve can be found from one of the two groups

in the example data set, which resulted in high accuracy. Similarly, the OPS in the medial region also showed high accuracy.

Figs. 11 and 8 together further demonstrate the correlation of the accuracy of the proposed method with the variability for each sulcus. Note that the identical sulcal regions in both figures received the same colors. Regions with low accuracy and high variability are colored red, while those with high accuracy and low variability are colored blue. For example, the ITS showed large incomplete errors (Fig. 11), and the variability for these sulci was also relatively large (Fig. 8). On the other hand, the CS and the CalcF exhibited low variability, for which our method worked with high accuracy.

Acknowledgments

This work was supported by Brain Korea Project, the School of Information Technology, KAIST in 2010, by the Korea Science and Engineering Foundation (KOSEF) grant funded by the Korea government (MEST) (2009-0077290), and by the Korea Science and Engineering Foundation (KOSEF) NRL program grant funded by the Korea government (MEST) (R0A-2007-000-20068-0). All opinions, findings, conclusions or recommendations expressed in this document are those of the author and do not necessarily reflect the views of the sponsoring agencies.

A

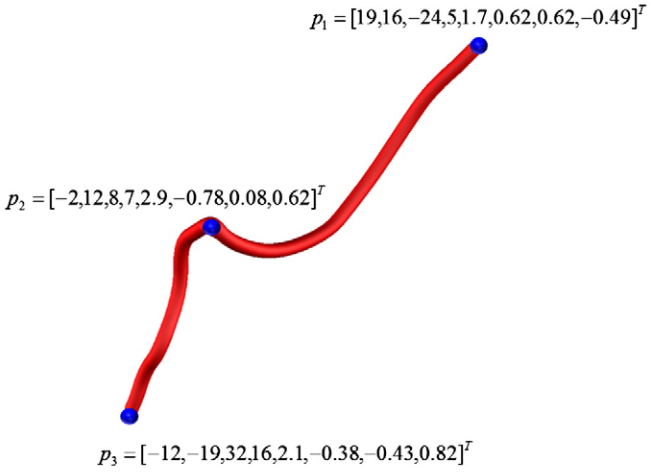

B

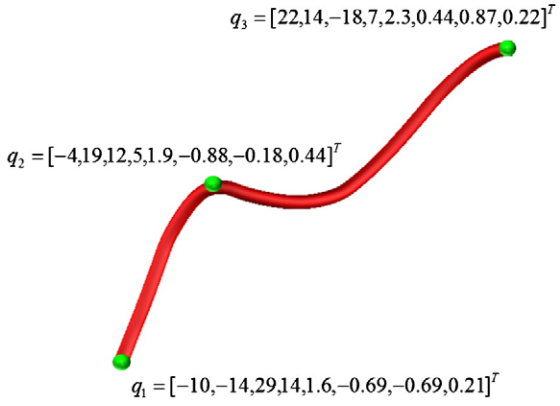

C

$$Assignments = \begin{cases} a_1 = (p_1, q_1) \\ a_2 = (p_1, q_2) \\ a_3 = (p_1, q_3) \\ a_4 = (p_2, q_1) \\ a_5 = (p_2, q_2) \\ a_6 = (p_2, q_3) \\ a_7 = (p_3, q_1) \\ a_8 = (p_3, q_2) \\ a_9 = (p_3, q_3) \end{cases} \quad M = \begin{bmatrix} 0.4016 & 0 & 0 & 0 & 0.4024 & 0.0867 & 0 & 0.1860 & 0.0304 \\ 0 & 0.5536 & 0 & 0.4814 & 0 & 0.1371 & 0.4944 & 0 & 0.0716 \\ 0 & 0 & 0.9101 & 0.5412 & 0.7156 & 0 & 0.7332 & 0.6504 & 0 \\ 0 & 0.4814 & 0.5412 & 0.7165 & 0 & 0 & 0 & 0.4278 & 0.1595 \\ 0.4024 & 0 & 0.7156 & 0 & 0.9031 & 0 & 0.9506 & 0 & 0.3440 \\ 0.0867 & 0.1371 & 0 & 0 & 0 & 0.6497 & 0.6169 & 0.5986 & 0 \\ 0 & 0.4944 & 0.7332 & 0 & 0.9506 & 0.6169 & 0.9265 & 0 & 0 \\ 0.1860 & 0 & 0.6504 & 0.4278 & 0 & 0.5986 & 0 & 0.70834 & 0 \\ 0.0304 & 0.0716 & 0 & 0.1595 & 0.3440 & 0 & 0 & 0 & 0.4273 \end{bmatrix}$$

$$Principal\ Eigenvector = [0.1052 \quad 0.1737 \quad \boxed{0.5145} \quad 0.2254 \quad \boxed{0.4710} \quad 0.2231 \quad \boxed{0.5316} \quad 0.2775 \quad 0.0860]^T$$

Fig. 15. An example to show an affinity matrix M using two simple sulcal curves: input and example sulcal curves p and q. Both the individual and pairwise affinity values are computed for nine possible assignments $a_k, k = 1,2,\cdots,9$, which are stored in the affinity matrix M. The principal eigenvector of the affinity matrix M is computed to determine the confidence of each assignment. In this example, we choose three pairs $(p_1,q_3),(p_2,q_2)$ and (p_3,q_1) as the consistent assignments.

Table 3
Labels and characteristics for major sulcal curves of human cerebral cortex.

Symbols	Labels	Locations	Remarks
STS	Superior temporal sulcus	Lateral	Continuous or 2–3 separate segments
ITS	Inferior temporal sulcus	Lateral	2–3 separate segments but continuous at times
CS	Central sulcus	Lateral	Usually continuous
PreCS	Precentral sulcus	Lateral	2–3 separate segments
PostCS	Postcentral sulcus	Lateral	Continuous or 2–3 separate segments
SFS	Superior frontal sulcus	Lateral	Continuous or discontinuous
IFS	Inferior frontal sulcus	Lateral	Highly likely not continuous
LTOS	Lateral temporo-occipital sulcus	Lateral	2–3 separate segments but continuous at times
MTOS	Medial temporo-occipital sulcus	Medial	Continuous or 2 separate segments
CingS	Cingulate sulcus	Medial	Continuous or 2 separate segments
CalcF	Calcarine fissure	Medial	Usually continuous
OPS	Occipito-parietal sulcus	Medial	Usually continuous

Appendix A

In this appendix, we present an example of constructing the affinity matrix M using two simple sulcal curves. Fig. 15 shows an input and an example sulcal curves, p and q, respectively. The 8D vector F is constructed at each of those feature points using Eq. (3). Consider three feature points $p_i, i=1,2,3$, and $q_j, j=1,2,3$ on the sulcal curve p and q, respectively. Those feature points give rise to nine possible assignments $a_k, k=1,2,\cdots,9$ (Fig. 15(C)): $a_1=(p_1,q_1)$, $a_2=(p_1,q_2)$, $a_3=(p_1,q_3)$, $a_4=(p_2,q_1)$, $a_5=(p_2,q_2)$, $a_6=(p_2,q_3)$, $a_7=(p_3,q_1)$, $a_8=(p_3,q_2)$, and $a_9=(p_3,q_3)$. The individual affinity values $M(a,a)$ are computed using Eq. (5), and stored along the diagonal of the affinity matrix M (Fig. 15(C)). The pairwise affinity values $M(a,b), a\neq b$ are computed using Eq. (7). Eq. (7) computes the pairwise symmetric affinity values, which results in a symmetric matrix M. As explained in the Spectral-based method section; however, the pairwise affinity value $M(a_1,a_2)$ is set to zero since assignments a_1 and a_2 are incompatible, that is, $p_1=p_1$ and $q_1\neq q_2$. Similarly, we set $M(a,b)=0$ for all incompatible pairs of assignments a and b. We then compute the principal eigenvector of the affinity matrix M (Fig. 15(C)). Each element of the eigenvector gives the confidence of the corresponding assignment between a pair of feature points. Let L be the set of all input-example feature point pairs: $L=\{(p_1,q_1),(p_1,q_2),(p_1,q_3),(p_2,q_1),(p_2,q_2),(p_2,q_3),(p_3,q_1),(p_3,q_2),(p_3,q_3)\}$. In order to construct the consistent assignment set C, we first choose the pair $a_7=(p_3,q_1)$ with the maximum confidence from L as an element of C (Fig. 15(C)). The pair (p_3,q_1) together with all conflicting pairs with this pair is removed from L, which results in $L=\{(p_1,q_2),(p_1,q_3),(p_2,q_2),(p_2,q_3)\}$ and $C=\{(p_3,q_1)\}$. For the remaining pairs in L, we repeat this process to choose the pair $a_3=(p_1,q_3)$, which makes $L=\{(p_2,q_2)\}$ and $C=\{(p_3,q_1),(p_1,q_3)\}$. Finally, what is left in L is the pair $a_5=(p_2,q_2)$ so as to obtain $L=\emptyset$ and $C=\{(p_3,q_1),(p_1,q_3),(p_2,q_2)\}$. We terminate this process since L becomes empty. Given the consistent assignment set C, the similarity A between two curves p and q is computed using Eq. (9):

$$\begin{aligned} A &= \sum_{a,b\in C} M(a,b) \\ &= M(a_7,a_7)+M(a_3,a_3)+M(a_5,a_5)+M(a_7,a_3)+M(a_7,a_5)+M(a_3,a_5) \\ &= 0.9265+0.9101+0.9031+0.7332+0.9506+0.7156 \\ &= 5.1391. \end{aligned}$$

Appendix B

Table 3 presents the major sulcal curves of a human cerebral cortex that we used and their characteristics.

References

Batchelor, P.G., Castellano Smith, A.D., Hill, D.L, Hawkes, D.J., Cox, T.C., Dean, A.F, 2002. Measures of folding applied to the development of the human fetal brain. IEEE Transactions on Medical Imaging 21, 953–965.

Behnke, K.J., Rettmann, M.E., Pham, D.L., Shen, D., Resnick, S.m., Davatzikos, C., Prince, J.l., May 2003. Automatic classification of sulcal regions of the human brain cortex using pattern recognition. In: Sonka, M., Fitzpatrick, J.M. (Eds.), Society of Photo-Optical Instrumentation Engineers (SPIE) Conference Series, Vol. 5032, pp. 1499-1510.

Besl, P., McKay, N., 1992. A method for registration of 3-D shapes. IEEE Trans. Pattern Anal. Mach. Intell. 14 (2), 239–256.

Cachia, A., Paillere-Martinot, M.L., Galinowski, A., Januel, D., De Beaurepaire, R., Bellivier, F., Artiges, E., Gallarda, T., Andoh, J., Bartres-Faz, D., Duchesnay, E., Riviere, D., Cointepas, Y., Plaze, M., Mangin, J.F., Martinot, J.L., 2008. Cortical folding abnormalities in schizophrenia patients with resistant auditory hallucinations. Neuroimage 39 (3), 927–935.

Caviness, V.S., Meyer, J., Makris, N., Kennedy, D.N., 1996. MRI-based topographic parcellation of human neocortex: an anatomically specified method with estimate of reliability. J. Cogn. Neurosci. 8 (6), 566–587.

Chui, H., Rangarajan, A., 2003. A new point matching algorithm for non-rigid registration. Comput. Vis. Image Underst. 89, 114–141.

Collins, D., Neelin, P., Peters, T., Evans, A., 1994. Automatic 3d intersubject registration of MR volumetric data in standardized Talairach space. J. Comput. Assist. Tomogr. 18, 192–205.

Cormen, T.H., Leiserson, C.E., Rivest, R.L., Stein, C., 2001. Introduction to Algorithms, 2nd ed. The MIT press.

Cykowski, M., Coulon, O., Kochunov, P., Amunts, K., Lancaster, J., Laird, A., Glahn, D., Fox, P., 2008a. The central sulcus: an observer-independent characterization of sulcal landmarks and depth asymmetry. Cerebral Cortex 18 (9), 1999–2009.

Cykowski, M.D., Kochunov, P., Ingham, R.J., Ingham, J.C., Mangin, J.F., Riviere, D., Lancaster, J., Fox, P.T., 2008b. Perisylvian sulcal morphology and cerebral asymmetry patterns in adults who stutter. Cereb. Cortex 18 (3), 571–583.

Damon, J., 2005. Determining the geometry of boundaries of objects from medial data. Int. J. Comput. Vision 63 (1), 45–64.

Dickinson, S., Pelillo, M., Zabih, R., 2001. Introduction to the special section on graph algorithms in computer vision. IEEE Trans. Pattern Anal. Mach. Intell. 23 (10), 1049–1052.

Douaud, G., Behrens, T.E., Poupon, C., Cointepas, Y., Jbabdi, S., Gaura, V., Golestani, N., Krystkowiak, P., Verny, C., Damier, P., Bachoud-Levi, A.C., Hantraye, P., Remy, P., 2009. In vivo evidence for the selective subcortical degeneration in Huntington's disease. Neuroimage 46 (4), 958–966.

Dubois, J., Benders, M., Borradori-Tolsa, C., Cachia, A., Lazeyras, F., Ha-Vinh Leuchter, R., Sizonenko, S., Warfield, S., Mangin, J.F., Huppi, P., 2008. Primary cortical folding in the human newborn: an early marker of later functional development. Brain 131 (8), 2028–2041.

Evans, A., Collins, D., Holmes, C., 1996. Computational approaches to quantifying human neuroanatomical variability. In: Mazziotta, J., Toga, A. (Eds.), Brain Mapping: The Methods. Academic Press.

Farin, G., 1988. Curves and Surfaces for Computer Aided Geometric Design: A Practical Guide. Academic Press Professional, Inc., San Diego, CA, USA.

Fillard, P., Arsigny, V., Pennec, X., Hayashi, K.M., Thompson, P.M., Ayache, N., 2007. Measuring brain variability by extrapolating sparse tensor fields measured on sulcal lines. NeuroImage 34 (2), 639–650.

Fischl, B., Salat, D.H., Busa, E., Albert, M., Dieterich, M., Haselgrove, C., van der Kouwe, A., Killiany, R., Kennedy, D., Klaveness, S., Montillo, A., Makris, N., Rosen, B., Dale, A.M., 2002. Whole brain segmentation: automated labeling of neuroanatomical structures in the human brain. Neuron 33 (3), 341–355.

Fischl, B., van der Kouwe, A., Destrieux, C., Halgren, E., Segonne, F., Salat, D.H., Busa, E., Seidman, L.J., Goldstein, J., Kennedy, D., Caviness, V., Makris, N., Rosen, B., Dale, A.M., 2004. Automatically parcellating the human cerebral cortex. Cereb. Cortex 14 (1), 11–22.

Fischl, B., Rajendran, N., Busa, E., Augustinack, J., Hinds, O., Yeo, B.T., Mohlberg, H., Amunts, K., Zilles, K., 2008. Cortical folding patterns and predicting cytoarchitecture. Cereb. Cortex 18 (8), 1973–1980.

Fitzpatrick, J., Hill, D., Shyr, Y., J., Studholme, C., Maurer, Jr., C.R., Aug. 2008. Visual assessment of the accuracy of retrospective registration of mr and ct images of the brain. IEEE Trans. Med. Imaging 17 (4), 571-585.

Goualher, G.L., Procyk, E., Collins, D., Venugopal, R., Barillot, C., Evans, A., March 1999. Automated extraction and variability analysis of sulcal neuroanatomy. IEEE Trans. Med. Imaging 18 (3), 206-217.

Hasnain, M., Fox, P., Woldorff, M., 2001. Structure–function spatial covariance in the human visual cortex. Cereb. Cortex 11, 702–716.

Hellier, P., Barillot, C., Feb. 2003. Coupling dense and landmark-based approaches for nonrigid registration. IEEE Trans. Med. Imaging 22 (2), 217-227.

Im, K., Lee, J.M., Lyttelton, O., Kim, S.H., Evans, A.C., Kim, S.I., 2008a. Brain size and cortical structure in the adult human brain. Cereb. Cortex 18 (9), 2181–2191.

Im, K., Lee, J.M., Seo, S., Lyttelton, O., Kim, S.H., Evans, A.C., Kim, S.I., 2008b. Sulcal morphology changes and their relationship with cortical thickness and gyral white matter volume in mild cognitive impairment and alzheimer's disease. Neuroimage 43, 103–113.

Im, K., Jo, H.J., Mangin, J.F., Evans, A.C., Kim, S.I., Lee, J.M., 2010. Spatial distribution of deep sulcal landmarks and hemispherical asymmetry on the cortical surface. Cerebral Cortex 20 (3), 602–611.

Jackowski, M., Kao, C.Y., Qiu, M., Constable, T.R., Constable, L.H., October 2005. White matter tractography by anisotropic wavefront evolution and diffusion tensor imaging. Med. Image Anal. 9 (5), 427-440.

Kao, C.Y., Hofer, M., Sapiro, G., Stern, J., Rehm, K., Rottenberg, D.A., 2007. A geometric method for automatic extraction of sulcal fundi. IEEE Trans. Med. Imaging 26 (4), 530–540.

Kim, J.S., Singh, V., Lee, J.K., Lerch, J., Ad-Dab'bagh, Y., MacDonald, D., Lee, J.M., Kim, S.I., Evans, A.C., 2005. Automated 3-d extraction and evaluation of the inner and outer cortical surfaces using a laplacian map and partial volume effect classification. NeuroImage 27 (1), 210–221.

Lee, J.K., Lee, J.M., Kim, J.S., Kim, I.Y., Evans, A.C., Kim, S.I., 2006. A novel quantitative cross-validation of different cortical surface reconstruction algorithms using MRI phantom. NeuroImage 31 (2), 572–584.

Leordeanu, M., Hebert, M., 2005. A spectral technique for correspondence problems using pairwise constraints. ICCV '05: Proceedings of the Tenth IEEE International Conference on Computer Vision. IEEE Computer Society, Washington, DC, USA, pp. 1482–1489.

Lohmann, G., Dec 1998. Extracting line representations of sulcal and gyral patterns in mr images of the human brain. IEEE Trans. Med. Imaging 17 (6), 1040-1048.

Lohmann, G., von Cramon, D., 2000. Automatic labelling of the human cortical surface using sulcal basins. Med. Image Anal. 4 (3), 179–188.

Lohmann, G., von Cramon, D.Y., Steinmetz, H., 1999. Sulcal variability of twins. Cereb. Cortex 9 (7), 754–763.

Lohmann, G., von Cramon, D.Y., Colchester, A.C.F., 2008. Deep sulcal landmarks provide an organizing framework for human cortical folding. Cereb. Cortex 18, 1415–1420.

Lyttelton, O., Boucher, M., Robbins, S., Evans, A., 2007. An unbiased iterative group registration template for cortical surface analysis. NeuroImage 34 (4), 1535–1544.

MacDonald, D., Kabani, N., Avis, D., Evans, A.C., 2000. Automated 3-d extraction of inner and outer surfaces of cerebral cortex from MRI. NeuroImage 12 (3), 340–356.

Mangin, J.F., Regis, J., Bloch, I., Frouin, V., Samson, Y., Lopez-Krahe, J., 1995. A MRF based random graph modelling the human cortical topography. CVRMed. 177–183.

Mazziotta, J.C., Toga, A.W., Evans, A., Fox, P., Lancaster, J., 1995. A probabilistic atlas of the human brain: theory and rationale for its development: the international consortium for brain mapping (ICBM). NeuroImage 2 (2, Part 1), 89–101.

Noblet, V., Heinrich, C., Heitz, F., Armspach, J.P., 2006. Retrospective evaluation of a topology preserving non-rigid registration method. Med. Image Anal. 10 (3), 366–384.

Ochiai, T., Grimault, S., Scavarda, D., Roch, G., Hori, T., Riviere, D., Mangin, J.F., Regis, J., 2004. Sulcal pattern and morphology of the superior temporal sulcus. NeuroImage 22 (2), 706–719.

Perrot, M., Riviere, D., Mangin, J.F., May 2008. Identifying cortical sulci from localizations, shape and local organization. 5th Proc. IEEE ISBI. Paris, France, pp. 420-423.

Pienaar, R., Fischl, B., Cariness, V., Makris, N., Grant, P.E, 2008. A methodology for analyzing curvature in the developing brain from preterm to adult. Int. J. Imaging Syst. Technol. Special Issue: Hum. Brain Imaging 18 (1), 42–68.

Pitiot, A., Delingette, H., Thompson, P.M., Ayache, N., 2004. Expert knowledge-guided segmentation system for brain MRI. NeuroImage 23 (Supplement 1), S85–S96 Mathematics in Brain Imaging.

Rademacher, J., Galaburda, A.M., Kennedy, D.N., Filipek, P.A., Caviness, V.S., 1992. Human cerebral cortex: localization, parcellation, and morphometry with magnetic resonance imaging. J. Cogn. Neurosci. 4 (4), 352–374.

Regis, J., Mangin, J.F., Ochiai, T., Frouin, V., Riviere, D., Cachia, A., Tamura, M., Samson, Y., 2005. "Sulcal root" generic model: a hypothesis to overcome the variability of the human cortex folding patterns. Neurol. Med. Chir. (Tokyo) 45, 1–17.

Rettmann, M.E., Han, X., Xu, C., Prince, J.L., 2002. Automated sulcal segmentation using watersheds on the cortical surface. NeuroImage 15 (2), 329–344.

Riviere, D., Mangin, J.F., Papadopoulos-Orfanos, D., Martinez, J.M., Frouin, V., Regis, J., 2002. Automatic recognition of cortical sulci of the human brain using a congregation of neural networks. Med. Image Anal. 6 (2), 77–92.

Riviere, D., Regis, J., Cointepas, Y., Papadopoulos-Orfanos, D., Cachia, A., Mangin, J.F., 2003. A freely available Anatomist/BrainVISA package for structural morphometry of the cortical sulci. Proc. 9th HBM. : Neuroimage, 19(2), p. 934. New York.

Robbins, S., Evans, A.C., Collins, D.L., Whitesides, S., 2004. Tuning and comparing spatial normalization methods. Med. Image Anal. 8 (3), 311–323.

Rodriguez-Carranza, C.E., Rousseau, F., Iordanora, B., Glen, O., Vigneron, D., Barkovich, J., Studholme, C, 2006. An iso-surface flooding analysis method applied to premature neonatal brain development. SPIE 6144.

Rusinkiewicz, Z., Sept. 2004. Estimating curvatures and their derivatives on triangle meshes. 3D Data Process., Vis. Transm. 2004, 486-493.

Sandor, S., Leahy, R., Feb. 1997. Surface-based labeling of cortical anatomy using a deformable atlas. IEEE Trans. Med. Imaging 16 (1), 41-54.

Seong, J.K., Im, K., Yoo, S.W., Seo, S.W., Na, D.L., Lee, J.M., 2010. Automatic extraction of sulcal lines on cortical surfaces based on anisotropic geodesic distance. NeuroImage 49 (1), 293–302.

Shi, Y., Thompson, P., Dinov, I., Toga, A., May 2008. Hamilton-Jacobi skeleton on cortical surfaces. IEEE Trans. Med. Imaging 27 (5), 664-673.

Shi, Y., Tu, Z., Reiss, A., Dutton, R., Lee, A., Galaburda, A., Dinov, I., Thompson, P., Toga, A., March 2009. Joint sulcal detection on cortical surfaces with graphical models and boosted priors. IEEE Trans. Med. Imaging 28 (3), 361-373.

Sled, J., Zijdenbos, A., Evans, A., Feb. 1998. A nonparametric method for automatic correction of intensity nonuniformity in MRI data. IEEE Trans. Med. Imaging 17 (1), 87-97.

Tao, X., Prince, J., Davatzikos, C., May 2002. Using a statistical shape model to extract sulcal curves on the outer cortex of the human brain. IEEE Trans. Med. Imaging 21 (5), 513-524.

Thompson, P.M., Schwartz, C., Lin, R.T., Khan, A.A., Toga, A.W., 1996a. Three-dimensional statistical analysis of sulcal variability in the human brain. J. Neurosci. 16 (13), 4261–4274.

Thompson, P.M., Schwartz, C., Toga, A.W., 1996b. High-resolution random mesh algorithms for creating a probabilistic 3D surface atlas of the human brain. NeuroImage 3 (1), 19–34.

Thompson, P.M., Hayashi, K.M., Sowell, E.R., Gogtay, N., Giedd, J.N., Rapoport, J.L., de Zubicaray, G.I., Janke, A.L., Rose, S.E., Semple, J., Doddrell, D.M., Wang, Y., van Erp, T. G., Cannon, T.D., Toga, A.W., 2004. Mapping cortical change in Alzheimer's disease, brain development, and schizophrenia. NeuroImage 23 (Supplement 1), S2–S18 mathematics in Brain Imaging.

Tu, Z., Zheng, S., Yuille, A., Reiss, A., Dutton, R., Lee, A., Galaburda, A., Dinov, I., Thompson, P., Toga, A., April 2007. Automated extraction of the cortical sulci based on a supervised learning approach. IEEE Trans. Med. Imaging 26 (4), 541-552.

Vaillant, M., Davatzikos, C., Bryan, R., Jun 1996. Finding 3D parametric representations of the deep cortical folds. Mathematical Methods in Biomedical Image Analysis, 1996, Proceedings of the Workshop on, 151-159.

Watkins, K., Paus, T., Lerch, J., Zijdenbos, A., Collins, D., Neelin, P., Taylor, J., Worsley, K., Evans, A., 2001. Structural asymmetries in the human brain: a voxel-based statistical analysis of 142 MRI scans. Cereb. Cortex 11 (9), 868–877.

Zijdenbos, A.P., Evans, A.C., Riahi, F., Sled, J.G., Chui, J., Kollokian, V., 1996. Automatic quantification of multiple sclerosis lesion volume using stereotaxic space. VBC '96: Proceedings of the 4th International Conference on Visualization in Biomedical Computing. Springer-Verlag, London, UK, pp. 439–448.